

Accepted version  
Licence CC BY-NC-ND

Please cite as:

Schito A, Romano C, Corrado S, Grigo D, Poe B (2017) "Diagenetic thermal evolution of organic matter by Raman spectroscopy", *Organic Geochemistry* 106, 57-67, doi: <http://dx.doi.org/10.1016/j.orggeochem.2016.12.006>

# 1 Diagenetic thermal evolution of organic matter by Raman spectroscopy

2 Andrea Schito <sup>a</sup>, Claudia Romano <sup>a</sup>, Sveva Corrado <sup>a</sup>, Domenico Grigo <sup>b</sup>, Brent Poe <sup>c</sup>

3 <sup>a</sup> Dipartimento di Scienze, Sezione di Scienze Geologiche, Università degli Studi Roma Tre, L.go S.  
4 Leonardo Murialdo 1, 00146, Roma, Italy

5 <sup>b</sup> Eni SpA e Exploration & Production Division, Via Emilia, San Donato Milanese, MI, 20097, Italy

6 <sup>c</sup> Dipartimento di Geotecnologie per l'Ambiente ed il Territorio, Università degli Studi "G. d'Annunzio" –  
7 Chieti, Via dei Vestini 30, 66013 Chieti Scalo, Italy

## 9 Corresponding author.

10 E-mail address: [andrea.schito@uniroma3.it](mailto:andrea.schito@uniroma3.it)

12 **Keywords:** thermal maturity; dispersed organic matter; Raman spectroscopy; diagenesis

## 14 Abstract

15 Vitrinite reflectance is considered one of the most reliable indicators of thermal maturity in sedimentary  
16 basins and is widely used to calibrate numerical models that assess hydrocarbon generation/expulsion from  
17 source rocks. Nevertheless, ambiguities in vitrinite reflectance can occur from variations in composition and  
18 preservation state of **organic facies**, temperature/ pressure conditions and **the abundance of** organic matter  
19 resulting in incorrect or uncertain assessments of petroleum systems.

20 **This study** presents an original application of Raman spectroscopy to assess the diagenesis - catagenesis of  
21 kerogen between the immature and mid-mature stages of hydrocarbon generation. Kerogens were isolated  
22 from 33 intervals of drill cuttings from a 5 km thick Oligocene-Miocene siliciclastic section of the Malembo  
23 Formation (Lower Congo Basin, Angola). Their Raman spectra were obtained and derived parameters were  
24 compared to depth and to previously reported equivalent vitrinite reflectance values. The best correlations  
25 between thermal maturity and Raman parameters were found for D-G band distance; FWHM of the G band;  
26 D/G area ratio; RA2 ratio (calculated as S+DI+SD/Dr+Gl+G band ratio) and the D/G width ratio. The  
27 Raman parameters were not influenced by varying kerogen composition (mixed type II/III). The technique  
28 offers the potential to reduce the risk of source rock thermal maturity assessment even when organic facies  
29 rich in amorphous organic matter are present.

## 32 1 Introduction

33 Quantitative evaluation of the thermal maturity of organic matter (OM) dispersed in sediments is a key  
34 element **in assessing the processes of** hydrocarbon (HC) generation/expulsion in petroleum systems. It is  
35 linked to the thermal evolution of sedimentary basins and orogenic belts (**Corrado et al., 2010**; Allen and  
36 Allen, 2013; Hackley and Cardott, 2016). Vitrinite reflectance analysis is considered a highly reliable and

37 reproducible measure of thermal maturity of coals. Its application to organic matter dispersed in sediments is  
38 a common practice, but there are inherent limitations that can lower the accuracy of the measurement. In  
39 many marine sediments, primary vitrinite macerals are absent or very sparse and it is often difficult to obtain  
40 **good results** without interference from eroded, secondary sources. Vitrinite reflectance in dispersed organic  
41 matter can also be effected **by other processes such as** oxidation during transport, preservation, and  
42 retardation and/or suppression. Numerical models calibrated against ambiguous vitrinite reflectance data can  
43 yield inaccurate or biased results. Alternative analytical techniques based on the analysis of both the organic  
44 and inorganic fraction of sediments can minimize these limitations (e.g., Aldega et al. 2007; Corrado et al.,  
45 2009; Federici et al., 2010; Di Paolo et al., 2012; Cantarelli et al., 2013; Andreucci et al., 2014; Schito et al.,  
46 2016).

47 Raman spectroscopy is a potential powerful non-destructive tool to quantitatively evaluate thermal maturity  
48 of organic matter (e.g., Beyssac et al., 2002; Quirico et al., 2005; Guedes et al., 2010, 2012; Lahfid et al.,  
49 2010; Liu et al., 2012, Hinrichs et al., 2014; Wilkins et al., 2014; Zhou et al., 2014; Lünsdorf, 2016; Mum  
50 and Inan, 2016; Ferralis et al., 2016). Advances in instrumentation and data processing have spurred  
51 increased applications, and the technique is now simple, fast and can be performed directly on standard  
52 petrographic thin sections or on bulk kerogen.

53 Specifically, two bands on Raman spectra, **namely G** (graphitic) and D (disordered), are related to the  
54 growth of the ordered domains with respect to the disordered ones in the organic matter (Tuinstra & Koenig,  
55 1970). Parameters linked to D and G bands have been used to show reliable correlations with  
56 paleotemperatures between 200 °C **and 650 °C** (Wopenka and Pasteris, 1993; Beyssac et al., 2002; Aoya et  
57 al., 2010; Lahfid et al., 2010; Endo et al., 2012) and against thermal maturity between 1 and 5-6 R<sub>o</sub>%  
58 (Kelemen and Fang, 2001; Jehlička et al., 2003; Quirico et al., 2005; Guedes et al., 2010; 2012; Liu et al.,  
59 2012; Hinrichs et al., 2014; Wilkins et al., 2014; Zhou et al., 2014; Lünsdorf, 2016; Mum and Inan, 2016).

60 The range of thermal maturity spanning **the** diagenetic to mid-catagenetic stages (corresponding to R<sub>o</sub>% 0.4-  
61 1.2) has been explored systematically in only a **few studies** (Wilkins et al., 2014; Hinrichs et al., 2016;  
62 Lünsdorf, 2016). These report considerable uncertainties at the **low** maturity stages, which are usually the  
63 most critical in constraining basin models.

64 In this **study**, we examine the applicability of Raman spectroscopy as a thermal indicator in the range  
65 between the immature and middle mature stages of HC generation, when applied to type II/III kerogen  
66 composed mainly **of** amorphous organic matter (AOM). We present the procedures and **analytical results**  
67 of the first order Raman spectra performed on Cenozoic organic matter dispersed in sediments of the  
68 Malembo Formation drilled in Lower Congo Basin (Angola) that records this maturity range. We  
69 demonstrate that robust parameterization of the thermal maturity of dispersed organic matter is possible  
70 using Raman indicators.

71

72

73 **2 Methods and Materials**

74 *2.1 Kerogen and thermal maturity*

75 Kerogen is the insoluble macromolecular fraction of sedimentary organic matter (Vandenbroucke and  
76 Largeau, 2007) and is the precursor of oil and gas resources. Dispersed OM is usually highly heterogeneous  
77 and reflects differences in its origin and preservation state. Different classifications of kerogen exist, based  
78 on optical analyses performed in reflected and transmitted light or rooted on bulk parameters, such as H/C  
79 and O/C atomic ratios or Hydrogen and Oxygen indexes derived from pyrolysis yields and TOC values.

80 In this work, we mainly refer to classifications based on optical organic petrography using transmitted light  
81 microscopy (Teichmüller, 1986; Tyson, 1995). Kerogen composition is classified into four classes from  
82 which the abundance and distribution of hydrogen-rich macerals can be discerned: 1) AOM: amorphous  
83 organic matter; 2) MPH: marine phytoplankton; 3) CWF: continental woody organic matter, namely  
84 phytoclasts; and 4) CHF: continental herbaceous fragments.

85 Analyses were performed on 33 samples originating from cuttings taken from a 5000 meter thick section  
86 drilled offshore Angola (Malembó Formation - Lower Congo Basin). The succession ranges from Oligocene  
87 to Upper Miocene and is composed mainly of organic-rich shales interbedded by nearshore to deepwater  
88 sandstones (Schito et al., 2016).

89 **Organic matter** of different origin and preservation state, detected through transmitted light analyses, were  
90 found in the upper section of the well (depth: 1290-3360m) where woody fragments (CWF) and herbaceous  
91 fragments (CHF) of **terrigenous** origin coexist with amorphous organic matter (AOM) and marine  
92 phytoplankton (MPH). In contrast, the lower part of the well (depth: 3600-4950 m) is mainly composed of  
93 amorphous organic matter with traces of bitumen (Table 1, Schito et al., 2016). Reflected light analyses on  
94 kerogen indicate that organic matter of woody fragments of continental origin are represented by vitrinite  
95 group macerals, whereas inertinite group macerals are totally absent (Table 1, Schito et al., 2016).

96 The maturation pattern of the well ranges between about 0.35 and 1.5 expressed as vitrinite reflectance  
97 values ( $R_o$ %) as reported in Corrado et al. (2016) and Schito et al. (2016).

98

99 *2.2 Sample preparation*

100 Kerogens were extracted using a wet-chemical acid demineralization **technique** according to Robl and Davis  
101 (1993) and Schimmelmann et al. (1999). Samples were lightly ground in an agate mortar for about 1 minute.  
102 Carbonates were dissolved by adding HCl on the dried samples. The HCl was added in small increments to  
103 prevent excessive foaming. Digestion of remaining silicates was done by adding a **mixture composed in equal**  
104 **parts by distilled water and HF concentrated at 40% weight percent** (45 ml) to 5 g of sample and placed on  
105 a shaker table for 2 hours. Kerogen isolates plus any acid-resistant minerals were recovered and washed 5-6  
106 times with distilled water.

107

108 *2.3 Raman Spectroscopy and curve fitting*

109 Raman spectroscopy was performed on the kerogen isolates using a Jobin Yvon micro-Raman LabRam system  
110 in a backscattering geometry. Data were collected over the range of 700-2300  $\text{cm}^{-1}$  (first order Raman

111 spectrum) using a 600 grooves/mm spectrometer gratings and CCD detector. A Neodimium-Yag laser at 532 nm  
112 (green laser) was used as the light source and optical filters adjusted the power of the laser (<0.4mW). The  
113 Raman backscattering was recorded after an integration time of 20 seconds for 6 repetitions for each  
114 measurement. This, together with the use of green laser and optical filters, allowed us to reduce the fluorescence  
115 background to minimal values. Between ten and fifteen measurements were performed for each samples to  
116 ensure reproducibility of measurements. Each organic grain was analysed with a 2  $\mu\text{m}$  diameter spot using a  
117 50 $\times$  optical power objective.

118 **Raman spectra** of highly disordered carbon materials, are affected by interference due to high fluorescence  
119 caused by the diffuse presence of hydrogen or residual mineral matter. The first step **in the analysis of** the  
120 spectra is the removal of the high fluorescence background by a baseline subtraction procedure. Once the  
121 procedure is optimized, it then must be reproduced for the entire set of samples.

122 Baseline subtraction was performed using a third order polynomial curve that best followed the real trend of the  
123 fluorescence in the most immature samples with high fluorescence background. In order to avoid errors induced  
124 by differences in the spectra range considered by the subtraction, we fixed baseline points at 1000 and 1850  $\text{cm}^{-1}$   
125 for all spectra. A polynomial curve was chosen with respect to the linear baseline because the latter tends to  
126 overestimate the D and G peaks intensities. We observed that the maximum difference resulting from baseline  
127 correction was detected for the D band intensity, whose values tend to be higher by 10-15 %.

128 After **removal of the background**, the spectra were deconvoluted using LabSpec 6 software by Horiba. As the  
129 Raman spectra of OM in diagenetic conditions show broad overlapping bands and multiple curve-fitting  
130 solutions exist (Lünsdorf and Lünsdorf, 2016), we **found** that the best solution using the minimum number of  
131 components was attained using a six band deconvolution with a mixed Gaussian-Lorentzian band profile. **The**  
132 **goodness of fit** is defined by the minimum values of the  $\chi^2$  value (less than 3 according to Sadezky et al., 2005).  
133 Several attempts to use only five bands fitting systematically provided  $\chi^2$  values two or three times higher than  
134 those obtained with a six bands approach. All spectra were deconvoluted using the six peak deconvolution  
135 procedure.

136

#### 137 *2.4 Band assignment for Raman spectra in dispersed organic matter*

138 The Raman spectral signal of kerogen is recorded in a “first order” region between 1000 and 2000  $\text{cm}^{-1}$  and  
139 “second order” region between 2000 and 3500  $\text{cm}^{-1}$ . Bands in the second order region are generally hidden  
140 by fluorescence for low mature samples (Beyssac et al., 2002) and were not observed in this study. The first  
141 order Raman spectra for **carbonaceous** materials consist of two main bands known as the D and G bands  
142 (Tuinstra and Koenig, 1970; Friedel and Carlson, 1972) and other bands that vary depending on the rank (Li,  
143 2007; Potgieter-Vermaak et al., 2011). The G band is the only Raman active vibration in crystalline graphite  
144 at 1582  $\text{cm}^{-1}$  (Tuinstra and Koenig, 1972; Reich and Thomsen, 2004; Pimenta, 2007) and is related to the in-  
145 plane vibration of the carbon atoms in the graphene sheets.

146 The D band at 1350  $\text{cm}^{-1}$  becomes active in disordered graphite and its frequency depends on the excitation  
147 laser (Pócsik et al., 1998). Its origin has been interpreted as a results of a double resonant Raman scattering

148 process (Pócsik et al., 1998; Reich and Thomsen, 2004; and Pimenta et al., 2007). Alternatively, the  
149 collective intensity of the D band **has been related** to the ring breathing vibration in the graphite sub-unit or  
150 polycyclic aromatic compounds (PAHs) (Negri et al., 2002;2004; Castiglioni et al., 2004; Di Donato et al.,  
151 2004; and Lünsdorf 2016) or to aromatics with 6 rings **or more** (Li, 2007).

152 When dealing with disordered materials, the contribution of other spectral features at 1100-1200  $\text{cm}^{-1}$  and  
153 1400-1500  $\text{cm}^{-1}$  cannot be neglected and even the assignment of the G and D bands to graphite vibrational  
154 modes is questionable. Unfortunately, **there have only been a few** attempt to explain the origin of these  
155 bands in disordered materials and these studies are often contradictory (Nemanich and Solin, 1979; Beny-  
156 Bassez and Rouzaud, 1985; Ferrari and Robertson, 2000; Castiglioni et al. 2004; Negri et al., 2004; Li et al.,  
157 2007; Rebelo et al. 2016). For this reason the assignment of Raman bands for disordered material is still a  
158 matter of debate.

159 In high-rank coals, Beyssac et al. (2002) observed the presence of two additional bands in the Raman  
160 spectrum: the D2 band, appearing as a right end shoulder of the G band at approximately 1620  $\text{cm}^{-1}$  and the  
161 D3 band, a wide band residing at approximately 1500  $\text{cm}^{-1}$ . These bands have been attributed to out-of-plane  
162 defects from tetrahedral carbons (Bèny-Bassez and Rouzaud, 1985), or to small crystallite size (Nemanich  
163 and Solin, 1979). Working on carbon material matured at lower temperatures (about 200-320°C), Lahfid et  
164 al. (2010) and Sadezky et al. (2005) proposed the presence of an additional band called D4 at about 1200  $\text{cm}^{-1}$ ,  
165 attributed to  $\text{sp}^3\text{-sp}^2$  bonds or C–C and C=C stretching vibrations of polyene-like structures.

166 In a recent study, Ferralis et al. (2016) found the presence of two bands as a broad shoulder of the D bands,  
167 called D4 at 1150  $\text{cm}^{-1}$  and D5 at 1250  $\text{cm}^{-1}$ . In Ferralis et al.'s (2016) work, the two bands **have been**  
168 **related to CH species in aliphatic hydrocarbon chains**. The authors confirm this hypothesis by showing a  
169 strong correlation between the intensity of D5 or D5+D4 band with the increase of the atomic ratio H:C in  
170 the range between almost pure graphite (H:C = 0.01) and weak metamorphosed kerogen (H:C = 0.65).

171 In low maturity coals, the Raman spectra of highly disordered carbonaceous matter are more complex.

172 In Li et al. (2006) and Li (2007), Raman spectra were deconvoluted into 10 bands. The authors attributed a  
173 band at about 1700  $\text{cm}^{-1}$  (G1 band) to a carbonyl group C=O, while the Gr (1540  $\text{cm}^{-1}$ ), V1 (1465  $\text{cm}^{-1}$ ) and  
174 Vr band (1380  $\text{cm}^{-1}$ ) which represent the “overlap” between D and G were assigned to mainly amorphous  
175 carbon structures in char, especially smaller ring systems (e.g., with 3-5 fused benzene rings). At lower  
176 wavenumbers, they found that the S band (1185  $\text{cm}^{-1}$ ), together with Sl band (~1220  $\text{cm}^{-1}$ ), acts as the  
177 shoulder of the **D band (1230  $\text{cm}^{-1}$ ) and mainly represents  $\text{C}_{\text{aromatic}}\text{-C}_{\text{alkyl}}$ , aromatic (aliphatic) ethers, C–**  
178 **C on hydroaromatic rings, hexagonal diamond carbon  $\text{sp}^3$  and C–H on aromatic rings.** Finally, the Sr band  
179 (1060  $\text{cm}^{-1}$ ) is assigned to C-H on aromatic rings and the R band (960-800  $\text{cm}^{-1}$ ) to C-C on alkanes and  
180 cyclic alkanes and/or C-H on aromatic rings.

181 **Similarly, based on analyses of carbon nanotubes, Rebelo et al. (2016) proposed new assignments for the**  
182 **first order Raman spectra. In their work the G band is fitted with a Lorentzian shape at ~1580  $\text{cm}^{-1}$**   
183 **surrounded by a Lorentzian Gr peak at ~1610  $\text{cm}^{-1}$  and a Gaussian G1 peak near 1500  $\text{cm}^{-1}$ . G1 band**  
184 **correspond to the same vibration of the G band in low size aromatic (Heise et al., 2009). The “D region”**

185 is deconvoluted to a central Lorentzian D band at 1350 cm<sup>-1</sup> and two satellites Gaussian band called D1  
186 and D2 (left and right) respectively at ~1250 and ~1400 cm<sup>-1</sup> that were assigned to identical vibrations of  
187 the D band, but in low size aromatic domains. Finally, a further band, the S band, was used to fit a  
188 relatively small feature on the left side of the spectra at around 1120cm<sup>-1</sup>.

189 Bands S and G1 were assigned to a fingerprint of polyacetylene-like structures or areas of conjugated double  
190 bonds mainly present along the borders of structures where aromaticity has been broken upon functionalization  
191 (Shirakawa et al., 1973).

192

### 193 2.5 Raman thermal maturity parameters

194 Debate still exists on how to relate Raman spectral features to carbonization ranks at low thermal maturity levels  
195 (Rantish et al., 2016). Tuinstra and Koenig (1970) proposed the relation  $ID/IG = C(vL)/La$  (TK relation), to  
196 study the **thermal evolution of carbonaceous materials**. ID/IG is the ratio between the intensities of the D and  
197 G peaks,  $La$  is the lateral dimension (parallel to the graphene planes) of the nanocrystal and  $C(vL)$  is a constant  
198 which depends on the laser frequency. Taking IG as a reference value, which is **independent** of the size of the  
199 crystal (Cançado et al., 2008), Tuinstra and Koenig (1970) found an inverse relation between the intensities of  
200 the D band and the crystal dimensions. Following the TK correlation, Wopenka & Pasteris (1993) correlated  
201 **certain** Raman parameters with metamorphic zonation as **determined** by mineral assemblages.

202 Subsequently, Yui et al. (1996) demonstrated the high sensitivity of some Raman parameters to metamorphic  
203 grade from low-grade to greenschist facies, while Beyssac et al. (2002) developed the so called RSCM  
204 geothermometer (Raman Spectroscopy of Carbonaceous Material). RSCM, which expresses a relationship  
205 between the Raman parameter R2 ( $R2 = D/([G + D + D2]$  area ratio) and metamorphic temperature, was  
206 initially calibrated in a range between 330-640°C, and later extended to contact- metamorphic rocks (Aoya et  
207 al., 2010) and low-grade metamorphism (Lahfid et al., 2010, RA1 and RA2 parameters; Lünsdorf, 2016).

208 **Given** the low temperature interval **covering** the sub-bituminous coal to the anthracite ranks, spectral features  
209 and **carbonization** are not so clearly correlated. In general, FWHM, **positions of** the G and D bands and D/G  
210 area ratio are the most **sensitive** parameters to maturation (Sadezky et al., 2005; Jehlicka et al., 2009; Marques  
211 et al., 2009; Guedes et al., 2010; Zhou et al., 2014; Hinrichs et al., 2016; Lünsdorf, 2016). Romero-Sarmiento et  
212 al. (2014) suggested that the FWHM of the G band shows the best correlation against **Rock-Eval** Tmax values  
213 in a set of samples from the Barnett shales (US), and Liu et al. (2012) determined thermal maturity by using the  
214 D-G distance in mature to highly mature carbonized samples of solid organic matter.

215

216

## 217 3 Results

### 218 3.1 Raman spectra

219 From a first qualitative assessment of spectral features, we **observed** a regular decrease of the fluorescence  
220 signal, **resulting in the reduction** of the slope of the spectra (Fig. 1), and a corresponding narrowing of the G  
221 bands along the same trend. We refer to Rebelo et al. (2016) for band nomenclature. Position and bands names

222 are shown in Figure 2a for **low maturity** OM and in Figure 2b for high maturity OM. Best fit results were  
223 achieved by considering S, DI and Dr as purely Gaussian, and D, G and GI as more mixed Gaussian-Lorentzian  
224 functions. **Generally**, in **response to increasing** thermal maturity, the width of the G band decreases, the D-G  
225 peak position difference increases and the GI area decreases.

226

### 227 *3.2 Correlation of Raman parameters against thermal maturity - Malembo Formation*

228 To correlate spectral features with thermal maturity, the following parameters were calculated: D and G  
229 position, D-G distance, full width at half maximum of the D and G bands (FWHM) and D/G intensity, area and  
230 full width at maximum height ratio. Moreover, we redefined the parameters RA1 and RA2 following the work  
231 of Lahfid et al. (2010), calculated as follows:

232 1)  $RA1 = \text{area}(S+DI+D) / \text{area}(S+DI+D+Dr+GI+G)$ ;

233 2)  $RA2 = \text{area}(S+DI+D) / \text{area}(Dr+GI+G)$ .

234 The D band position decreases slightly with depth from about 1380  $\text{cm}^{-1}$  to 1360  $\text{cm}^{-1}$ , while the G band position  
235 (Fig. 3a) shows no trends with depth, ranging between 1590  $\text{cm}^{-1}$  and 1600  $\text{cm}^{-1}$  (Fig. 3b). As a consequence, the  
236 D-G difference increases slightly with depth from about 220  $\text{cm}^{-1}$  to 240  $\text{cm}^{-1}$  (Fig 3c).

237 The full width at half maximum (FWHM) of the D band ranges between 90  $\text{cm}^{-1}$  and 110  $\text{cm}^{-1}$  with no defined  
238 trend, while the full width at half maximum (FWHM) of the G band decreases from about 90  $\text{cm}^{-1}$  to 55  $\text{cm}^{-1}$   
239 (Fig.3d-e). The intensity ratio between the D and G bands does not show any correlation with depth (Fig. 3f),  
240 while the D/G area ratio and full width at maximum height ratio shows a trend of increasing values with depth,  
241 ranging from about 0.5 to 1.0 and 1.0 and 1.8, respectively (Fig. 3g-h). Both RA1 and RA2 show values ranging  
242 from 0.35 to 0.50 for RA1 and from about 0.55 to 1.10 for RA2 (Fig. 3i-j). **The** best correlations with depth are  
243 provided by the D-G difference (Fig. 3c), the FWHM of peak G (Fig. 3e), the D/G area ratio (Fig. 3g), D/G  
244 width ratio (Fig. 3h) and the RA2 parameter (Fig. 3j).

245 We plotted these parameters against the maturity profile of the well expressed in  $R_o\%$  (for details see Schito  
246 et al., 2016) in Fig. 4. A power equation was used to fit the D/G area ( $R^2 = 0.93$ ), RA2 ( $R^2 = 0.95$ ) and D/G  
247 width ( $R^2 = 0.96$ ) parameters (Fig.4c-d-e), FWHM-G parameter ( $R^2 = 0.91$ ) and the D-G distance ( $R^2 = 0.94$ )  
248 were fitted according to a second order polynomial equation (Fig. a-b).

249

250

## 251 **4 Discussions**

252 **We observed** good correlations between Raman parameters and well depth for kerogens from the Cenozoic  
253 Malembo Formation (Lower Congo Basin, Angola) **in our study**. The Raman parameters also correlate very  
254 well with vitrinite reflectance values reported by Schito et al. (2016), which range from about 0.3% to about  
255 1.5%  $R_o$ . In the investigated well, Raman spectral features vary continuously with depth independent of  
256 **kerogen** composition. This is in general agreement with Chen et al. (2012) **who showed that** differences in  
257 parameters derived from micro-FT-IR analyses on vitrinite and liptinite macerals (e.g., AOM) were



258 negligible. Raman spectra parameters that best correlate against thermal maturity are: 1) D and G band  
259 position difference; 2) G band FWHM and 3) D and G bands area/width ratio (including the RA2 parameter).

260

#### 261 *4.1 Distance between D and G bands*

262 The shift in position of the D and G bands is related to processes that occur at different carbonization ranks.  
263 According to Ferrari and Robertson (2000), the D band shift toward lower wavenumbers is attributable to the  
264 increase of larger aromatic clusters passing from disordered to more ordered materials.

265 The increase of the D-G distance with thermal maturity is mainly driven by the shift of the D position toward  
266 lower wavenumbers (Fig. 3a), while no apparent trend is visible for the G position (Figure 3b). This  
267 observations are in agreement with those made others (Ferrari and Robertson, 2000; Kelemen and Fang,  
268 2001; Nestler et al., 2003; Quirico et al., 2005; Guedes et al., 2010; and Liu et al, 2012). The D-G distance is  
269 one of the best parameters to correlate against vitrinite reflectance (Fig. 4a). Our results are in agreement  
270 with Kelemen and Fang (2001) and Liu et al. (2012) (for samples with R<sub>o</sub>% varying between 0.5% and **4%**).

271

#### 272 *4.2 Full Width at Half Maximum of the G band*

273 According to Ferrari and Robertson (2000), the width of the G peak increases as a function of the bond-angle disorder at  
274 sp<sup>2</sup> sites (in aromatic rings and olefinic) and its values are the greatest for high sp<sup>3</sup> sites content (aliphatic chains) in  
275 highly disordered materials. This parameter increases as a function of decreasing temperature or thermal maturity in  
276 regional metamorphism (Beyssac et al., 2002; Lahfid et al., 2010) and progressive coalification (Ferrari and Robertson,  
277 2000; **Kelemen and Fang, 2001**; Jehlička et al., 2003; **Quirico et al., 2005**; Marques et al., 2009; **Guedes et al., 2010a**  
278 ; Wilkins et al., 2014, Hinrichs et al., 2016). In agreement with existing studies, we observed a decrease of FWHM-G as  
279 a function of increasing R<sub>o</sub>% (Figs. 4b). According to spectra deconvolution, the overall decrease in the  
280 integrated intensity of the G region is attributable to both a decrease in the FWHM of the G band and to a  
281 decrease in area of the GI band (Fig. 5). This is in good agreement with the assignment of the GI band to  
282 polyacetylene-like structures (e.g., polyene chains) **which** are expected to decrease as thermal maturity  
283 increases (**Castiglioni et al., 2004**; Rebelo et al., 2016 ). Similar behaviour **is seen in** the Gr (1540 cm<sup>-1</sup>) and  
284 VI (1465 cm<sup>-1</sup>) of Li et al. (2007), assigned to mainly amorphous carbon structures in char, especially smaller  
285 ring systems (e.g., with 3-5 fused benzene rings) **which** also are expected to decrease as thermal maturity  
286 increases.

287

#### 288 *4.3 Area and width ratio parameters (D/G area, RA2, D/G width)*

289 **The intensity ratio between D and G bands**, is related to the in-plane crystallite size (Tuinstra and  
290 Koenig, 1976) in disordered graphite and shows an inverse correlation against paleotemperatures between  
291 330-650 °C (Beyssac et al., 2002). The same relationship is not **seen at low temperatures** (Ferrari and  
292 Robertson, 2000) and the area ratio of D and G bands and parameters related to this ratio (RA1 and RA2,  
293 Lahfid et al., 2010) correlate **better** against temperature and thermal maturity (Kelemen and Fang, 2001;  
294 Jehlička et al., 2003; Quirico et al., 2005; Sadezky et al., 2005; Marques et al., 2009; Guedes et al., 2010; Liu

295 et al., 2012). This is probably due to the fact that while the intensity ratio behaves similarly to the D/G area  
296 ratio for disordered graphite, this correlation is no longer valid for amorphous carbon where the width of  
297 both bands are related to the disorder in the structure (Ferrari and Robertson, 2000).

298 We observe that the ID/IG ratio does not correlate with depth (Fig. 3f) or  $R_o\%$  while D/G area and width  
299 ratio (Figs. 3g) and RA1 and RA2 parameters (Figs. 3i - j) increase linearly with thermal maturity. The  
300 increase in D/G area and width ratio and in RA1 and RA2 parameters are partially attributable to the thinning  
301 of the G band due to the clustering of the aromatic rings (Ferrari and Robertson, 2000; Li et al., 2007) and  
302 also to the decrease in intensity of peak G1 (Fig. 5). However, other contributions may **also** be important to  
303 consider. For this reason, in order to understand and isolate the contribution of each single band to the  
304 RA1 and RA2 variation in our set of samples, we normalized each band to the G band intensity in Figure 6,  
305 where the ratio between the G band intensity and the area of the D, S, D1 and Dr bands against an increasing  
306 maturation pattern on the x axes is presented. **No significant** variations are observed in the IG/S area or in  
307 the IG/D1 area ratio, while a decrease in the IG/D area (e.g., D area band increase) and an increase of the  
308 IG/Dr area ratio (e.g., Dr band area decrease) are clearly visible.

309 We conclude that the increase in RA2 ratio is attributed to the decrease in width and intensity of G and G1  
310 bands and to the decrease of the satellite band Dr. **This is** accompanied by a corresponding increase in D  
311 band area (IG/D area decrease) **which is mostly** due to an increase in FWHM of the D band (Fig 3d).

312 While the D band increases, the G, G1 and Dr decrease with increasing structural ordering, in agreement with  
313 the interpretations already proposed by Ferrari and Robertson (2000), Li et al., (2007) and Rebelo et al.  
314 (2015). The interpretation of the Dr and S bands is not straightforward. Rebelo et al. (2015) assign these  
315 bands (S and D1) to the same vibrational modes and to the same structural units of G1 and Dr bands,  
316 respectively; thus, we would expect similar coupled behaviour for these bands at increasing temperature.  
317 However, we observe a decoupling between S and G1 and D1 and Dr bands with temperature.

318 A similar decoupling was observed by Ferralis et al. (2016) who suggested a different origin for the S and D1  
319 bands (called the D4 and D5 bands in Ferralis et al., 2016). The authors observed that in the 1200  $\text{cm}^{-1}$  - 1300  
320  $\text{cm}^{-1}$  region the D4 and D5 bands are **related** to deformation modes of C-C (D4) and CH (D5) species  
321 associated with long saturated and unsaturated alkane chains. These bands show an intensity increase with  
322 the increase of H:C ratio from weakly metamorphosed kerogen to graphite.

323 On the other hand, no trend is observed for the S and D1 bands in Figure 6. This could be due to the different  
324 composition of the OM in the upper part of the well (**varying terrigenous OM** and AOM enrichment)  
325 generating different responses of the excitation bands with increasing thermal maturity. The variation of C-C  
326 and C-H associated with aliphatic at low maturity stages ( $R_o\% < 1.5$ ) is not straightforward and depends on  
327 complex chemical changes that occur simultaneously, such as shortening of aliphatic chains, decreased  
328 branching of aliphatic chains and formation of cyclic compounds (Lis et al., 2005). Therefore, we infer that  
329 the assignment of the S and D1 bands is still unclear and further investigations are strongly needed to fully  
330 address this issue.

331

### 332 4.3 Raman spectra evolution in Organic matter

333 Comparing our results with those obtained at higher degrees of maturation (Beyssac et al., 2002; Lahfid et  
334 al., 2010 and Rantish et al., 2016), we can trace the evolution of Raman spectra of the OM over a wide range  
335 of paleotemperatures. Using data from previous studies, we observed the **following changes going from**  
336 **anthracite to graphite ranks** (i.e. typically greenschist facies and above, see Wopenka and Pasteris, 1993;  
337 Beyssac et al., 2002): a decrease in the D band area, a shrinking of the G band and a shift of the G band  
338 toward the triperiodic graphite position (Fig. 7). **Conversely, going from low volatile bituminous coal to**  
339 **anthracite ranks, we observed from the works of Lahfid et al., (2010), Hinrichs et al., (2016) and**  
340 **Lünsdorf, (2016) an increase of the D band and a progressive disappearance of the minor bands.**  
341 **From results from this work, we found that changes in Raman spectra in diagenesis consist mainly in a**  
342 **narrowing of the G band region and a small increase of the D band area.** The decrease of the G band  
343 area is due to a progressive **shrinking** of the G band and to the decrease in the area of the G1 and Dr bands  
344 assigned to small aromatic rings and small polyene domains present only in kerogen at low thermal maturity  
345 levels (Castiglioni et al., 2004; Li et al., 2007; Rebelo et al., 2016).

346

347

### 348 5 Conclusions

349 Raman spectroscopic measurements **were performed** on shales collected **from** a 5 km deep well drilled  
350 across the Miocene-Oligocene Malembo Formation in the Lower Congo Basin (offshore of Angola). **Bulk**  
351 kerogens, with a thermal maturity **range** increasing from about 0.3 R<sub>o</sub>% at the top of the well to about 1.5  
352 R<sub>o</sub>% at the bottom were analysed.

353 The best correlations of Raman spectral parameters against the increase of thermal maturity are: D-G band  
354 distance; FWHM of the G band; D/G area ratio; RA2 ratio (calculated as S+Dl+SD/Dr+G1+G band ratio) and  
355 the D/G width ratio.

356 These results demonstrate that, at low diagenetic stages (between **the** immature and mid-mature stages of  
357 hydrocarbon generation) changes in Raman spectra of undifferentiated dispersed organic matter **show**  
358 quantifiable changes in response to thermal maturation and can be used to successfully parameterize the  
359 thermal evolution of a sedimentary succession.

360

### 361 Acknowledgments

362 We are greatly indebted to ENI for providing cuttings analysed in this work and permission to publish  
363 transmitted light analysis data on kerogen. Organic matter analyses were performed at the EVPL and ALBA  
364 (Roma Tre University) and at the ENI laboratories of Bolgiano (S. Donato Milanese). Donato Barbieri, Lea  
365 di Paolo and Roberto Galimberti (ENI) are kindly acknowledged for stimulating discussions on organic  
366 matter thermal evolution. This research was funded by: MIUR grants to Roma Tre PhD School in Earth  
367 Sciences (XXVIII doctoral cycle, 2013-2015).

368

369

### 370 References

371

372 Aldega, L., Corrado, S., Grasso, M., Maniscalco, R., 2007. Correlation of diagenetic data from organic and  
373 inorganic studies in the Apenninic-Maghrebian fold-and-thrust belt: a case study from eastern Sicily. *The*  
374 *Journal of Geology* 115, 335-353.

375  
376 Allen, P. A., Allen, J. R., 2013. *Basin Analysis: Principles and Application to Petroleum Play Assessment*,  
377 third ed. John Wiley & Sons, Hoboken, NJ, USA.

378  
379 Andreucci, B., Castelluccio, A., Corrado, S., Jankowski, L., Mazzoli, S., Szaniawski, R., Zattin, M., 2015.  
380 Interplay between the thermal evolution of an orogenic wedge and its retro-wedge basin: An example from  
381 the Ukrainian Carpathians. *Geological Society of America Bulletin* 127, 410-427.

382  
383 Aoya, M., Kouketsu, Y., Endo, S., Shimizu H., Mizukami, T., Nakamura, D., Wallis, S., 2010. Extending the  
384 applicability of the Raman carbonaceous-material geothermometer using data from contact metamorphic  
385 rocks. *Journal of Metamorphic Geology* 28, 895-914.

386  
387 Beny-Bassez, C., Rouzaud, J., 1985. Characterization of carbonaceous materials by correlated electron and  
388 optical microscopy and Raman microspectroscopy. *Scanning Electron Microscopy* 1, 119-132.

389  
390 Beyssac, O., Goff , B., Chopin, C., Rouzaud, J., 2002. Raman spectra of carbonaceous material in  
391 metasediments: a new geothermometer. *Journal of metamorphic Geology* 20, 859-871.

392  
393 Beyssac, O., Goff , B., Petitet, J.-P., Froigneux, E., Moreau, M., Rouzaud, J.-N., 2003. On the  
394 characterization of disordered and heterogeneous carbonaceous materials by Raman spectroscopy.  
395 *Spectrochimica Acta Part A: Molecular and Biomolecular Spectroscopy* 59, 2267-2276.

396  
397 **Can ado, L., Takai, K., Enoki, T., Endo, M., Kim, Y., Mizusaki, H., Speziali, N., Jorio, A., Pimenta,**  
398 **M., 2008. Measuring the degree of stacking order in graphite by Raman spectroscopy. *Carbon* 46, 272-**  
399 **275.**

400  
401 Cantarelli, V., Aldega, L., Corrado, S., Invernizzi, C., Casas-Sainz, A., 2013. Thermal history of the Arag n-  
402 B arn Basin (Late Paleozoic, western Pyrenees, Spain); insights into basin tectonic evolution. *Italian Journal*  
403 *of Geosciences* 132, 443-462.

404  
405 Caricchi, C., Corrado, S., Di Paolo, L., Aldega, L., Grigo, D., 2016. Thermal maturity of Silurian deposits in  
406 the Baltic Syneclise (on-shore Polish Baltic Basin): contribution to unconventional resources assessment.  
407 *Italian Journal of Geosciences* 135, 383-393.

408  
409 Carr, A.D., 2000. Suppression and retardation of vitrinite reflectance, Part 1. Formation and significance for  
410 hydrocarbon generation. *Journal of Petroleum Geology* 23, 313-343.

411  
412 Castiglioni, C., Tommasini, M., Zerbi, G., 2004. Raman spectroscopy of polyconjugated molecules and  
413 materials: confinement effect in one and two dimensions: *Philosophical Transactions of the Royal Society of*  
414 *London. Series A. Mathematical, Physical and Engineering Sciences* 362, 2425-2459.

415  
416 Corrado, S., Aldega, L., Balestrieri, M.L., Maniscalco, R., Grasso, M., 2009. Structural evolution of the  
417 sedimentary accretionary wedge of the Alpine system in eastern Sicily: thermal and thermochronological  
418 constraints. *Geological Society of America Bulletin* 121, 1475-1490.

419  
420 Corrado, S., Aldega, L., Zattin, M., 2010. Sedimentary vs. tectonic burial and exhumation along the  
421 Apennines (Italy). *Journal of the Virtual Explorer* 36,1-37.

422  
423 Corrado, S., Schito, A., Aldega, L., Grigo, D., 2016. A quantitative multi-method approach to assess thermal  
424 evolution of the Lower Congo Basin (Angola). *Rendiconti Online della Societ  Geologica Italiana* 40,  
425 pp.525.

426

427 Di Paolo, L., Aldega, L., Corrado, S., Mastalerz, M., 2012. Maximum burial and unroofing of Mt. Judica  
428 recess area in Sicily: implication for the Apenninic–Maghrebian wedge dynamics. *Tectonophysics* 530, 193-  
429 207.

430

431 **Di Donato, E., Tommasini, M., Fustella, G., Brambilla, L., Castiglioni, C., Zerbi, G., Simpson, C.D.,**  
432 **Müllen, K., Negri, F., 2004. Wavelength-dependent Raman activity of D2h symmetry polycyclic**  
433 **aromatic hydrocarbons in the D-band and acoustic phonon regions. *Chemical Physics* 301, 81–93.**  
434

435 **Endo, S., Wallis, S. R., Tsuboi, M., Torres De Leòn, R., Solari, L. A., 2012. Metamorphic evolution of**  
436 **lawsonite eclogites from the southern Motagua fault zone, Guatemala: insights from phase equilibria**  
437 **and Raman spectroscopy. *Journal of Metamorphic Geology* 30, 143-164.**  
438

439 **Federici, I., Cavazza, W., Okay, A. I., Beyssac, O., Zattin, M., Corrado, S. Dellisanti, F., 2010.**  
440 **Thermal Evolution of the Permo-Triassic Karakaya Subduction-accretion Complex between the Biga**  
441 **Peninsula and the Tokat Massif (Anatolia). *Turkish Journal of Earth Sciences* 19, 409-429.**  
442

443 **Ferrari, A.C., Robertson, J., 2000. Interpretation of Raman spectra of disordered and amorphous**  
444 **carbon: *Physical Review B* 61, 14095-14107.**  
445

446 Ferrari, A. C., Robertson, J., 2004. Raman spectroscopy of amorphous, nanostructured, diamond-like  
447 carbon, and nanodiamond. *Philosophical Transactions of the Royal Society of London A: Mathematical,*  
448 *Physical and Engineering Sciences* 362, 2477-2512.

449

450 Friedel, R., Carlson, G., 1972. Difficult carbonaceous materials and their infra-red and Raman spectra.  
451 Reassignments for coal spectra. *Fuel* 51, 194-198.

452

453 Guedes, A., Valentim, B., Prieto, A. C., Rodrigues, S., Noronha, F., 2010. Micro-Raman spectroscopy of  
454 collotelinite, fusinite and macrinite. *International Journal of Coal Geology* 83, 415-422.

455

456 Guedes, A., Valentim, B., Prieto, A., Noronha F., 2012. Raman spectroscopy of coal macerals and fluidized  
457 bed char morphotypes. *Fuel* 97, 443-449.

458

459 Hackley, P. C., Cardott, B. J., 2016. Application of organic petrography in North American shale petroleum  
460 systems: A review. *International Journal of Coal Geology* 163, 8-51.

461

462 **Heise, H., Kuckuk, R., Ojha, A., Srivastava, A., Srivastava, V., Asthana, B., 2009. Characterisation of**  
463 **carbonaceous materials using Raman spectroscopy: a comparison of carbon nanotube filters,**  
464 **single-and multi-walled nanotubes, graphitised porous carbon and graphite. *Journal of Raman***  
465 **Spectroscopy** 40, 344-353.  
466

467 Jehlička, J., Urban, O., Pokorný, J., 2003. Raman spectroscopy of carbon and solid bitumens in sedimentary  
468 and metamorphic rocks. *Spectrochimica Acta Part A: Molecular and Biomolecular Spectroscopy* 59, 2341-  
469 2352.

470

471 Jehlička, J., Šťastná, A., Přikryl, R., 2009. Raman spectral characterization of dispersed carbonaceous matter  
472 in decorative crystalline limestones. *Spectrochimica Acta Part A: Molecular and Biomolecular Spectroscopy*  
473 73, 404-409.

474

475 Kelemen, S., Fang, H., 2001, Maturity trends in Raman spectra from kerogen and coal. *Energy & Fuels* 15,  
476 653-658.

477

478 Lahfid, A., Beyssac, O., Deville, E., Negro, F., Chopin, C., Goffé, B., 2010. Evolution of the Raman  
479 spectrum of carbonaceous material in low-grade metasediments of the Glarus Alps (Switzerland). *Terra*  
480 *Nova* 22, 354-360.

481

482 Li, C.-Z., 2007. Some recent advances in the understanding of the pyrolysis and gasification behaviour of  
483 Victorian brown coal. *Fuel* 86, 1664-1683.  
484

485 Lis, G. P., Mastalerz, M., and Schimmelmann, A., 2008, Increasing maturity of kerogen type II reflected by  
486 alkylbenzene distribution from pyrolysis-gas chromatography–mass spectrometry: *Organic Geochemistry* 39,  
487 440-449.  
488

489 Liu, D., Xiao, X., Tian, H., Min, Y., Zhou, Q., Cheng, P., Shen, J., 2012. Sample maturation calculated using  
490 Raman spectroscopic parameters for solid organics: Methodology and geological applications. *Chinese*  
491 *Science Bulletin* 58, 1285-1298.  
492

493 Lünsdorf, N. K., 2016. Raman spectroscopy of dispersed vitrinite - Methodical aspects and correlation with  
494 reflectance. *International Journal of Coal Geology* 153, 75-86.  
495

496 Marques, M., Suárez-Ruiz, I., Flores, D., Guedes, A., Rodrigues, S., 2009. Correlation between optical,  
497 chemical and micro-structural parameters of high-rank coals and graphite. *International Journal of Coal*  
498 *Geology* 77, 377-382.  
499

500 Mumm, A. S., İnan, S., 2016. Microscale Organic Maturity determination of Graptolites using  
501 Raman Spectroscopy. *International Journal of Coal Geology* 162, 96-107.  
502

503 Negri, F., di Donato, E., Tommasini, M., Castiglioni, C., Zerbi, G., Müllen, K., 2004. Resonance Raman  
504 contribution to the D band of carbon materials: modeling defects with quantum chemistry. *Journal of*  
505 *Chemical Physics* 120, 11889–11900.  
506

507 Nemanich, R., Solin, S., 1979. First-and second-order Raman scattering from finite-size crystals of graphite.  
508 *Physical Review B* 20, 392.  
509

510 Nestler, K., Dietrich, D., Witke, K., Rößler, R., Marx, G., 2003. Thermogravimetric and Raman  
511 spectroscopic investigations on different coals in comparison to dispersed anthracite found in permineralized  
512 tree fern *Psaronius* sp. *Journal of Molecular Structure* 661, 357-362.  
513

514 Petersen, H., Rosenberg, P., 1998. Reflectance retardation (suppression) and source rock properties related to  
515 hydrogen enriched vitrinite in middle Jurassic coals, Danish North Sea. *Journal of Petroleum Geology* 21,  
516 247-263.  
517

518 Potgieter-Vermaak, S., Maledi, N., Wagner, N., Van Heerden, J., Van Grieken, R., Potgieter, J., 2011.  
519 Raman spectroscopy for the analysis of coal: a review. *Journal of Raman Spectroscopy* 42, 123-129.  
520

521 Pócsik, I., Hundhausen, M., Koós, M., Ley, L., 1998. Origin of the D peak in the Raman spectrum of  
522 microcrystalline graphite. *Journal of Non-Crystalline Solids* 227, 1083-1086.  
523

524 Price, L. C., Barker, C. E., 1985. Suppression of vitrinite reflectance in amorphous rich kerogen--a major  
525 unrecognized problem. *Journal of Petroleum Geology* 8, p. 59-84.  
526

527 Quirico, E., Rouzaud, J. N., Bonal, L., Montagnac, G., 2005. Maturation grade of coals as revealed by  
528 Raman spectroscopy: progress and problems. *Spectrochimica Acta Part A: Molecular and Biomolecular*  
529 *Spectroscopy* 61, 2368-2377.  
530

531 Rantitsch, G., Lämmerer, W., Fisslthaler, E., Mitsche, S., Kaltenböck, H., 2016. On the discrimination of  
532 semi-graphite and graphite by Raman spectroscopy. *International Journal of Coal Geology* 159, 48–56.  
533

534 Rebelo, S. L., Guedes, A., Szcfczyk, M. E., Pereira, A. M., Araújo, J. P., Freire, C., 2016. Progress in the  
535 Raman spectra analysis of covalently functionalized multiwalled carbon nanotubes: unraveling disorder in  
536 graphitic materials. *Physical Chemistry Chemical Physics* 18, 12784-12796.  
537

- 538 Robl, T. L., Davis, B. H., 1993. Comparison of the HF-HCl and HF-BF<sub>3</sub> maceration techniques and the  
539 chemistry of resultant organic concentrates. *Organic Geochemistry* 20, 249-255.  
540
- 541 Romero-Sarmiento, M.-F., Rouzaud, J.-N., Bernard, S., Deldicque, D., Thomas, M., Littke, R., 2014.  
542 Evolution of Barnett Shale organic carbon structure and nanostructure with increasing maturation. *Organic*  
543 *Geochemistry* 71, 7-16.  
544
- 545 Sadezky, A., Muckenhuber, H., Grothe, H., Niessner, R., Pöschl, U., 2005. Raman microspectroscopy of  
546 soot and related carbonaceous materials: Spectral analysis and structural information. *Carbon* 43, 1731-1742.  
547
- 548 **Schito, A., Corrado, S., Aldega, L., Grigo, D., 2016. Overcoming pitfalls of vitrinite reflectance**  
549 **measurements in the assessment of thermal maturity: the case history of the lower Congo basin.**  
550 ***Marine and Petroleum Geology* 74, 59-70.**  
551
- 552 Scott, A. C., Glasspool, I. J., 2007. Observations and experiments on the origin and formation of inertinite  
553 group macerals. *International Journal of Coal Geology* 70, 53-66.  
554
- 555 Shirakawa, H., Ito, T., Ikeda, S., 1973. Raman scattering and electronic spectra of poly (acetylene). *Polymer*  
556 *Journal* 4, 460-462.  
557
- 558 Taylor, G. H., 1998. *Organic petrology: A new handbook incorporating some revised parts of Stach's*  
559 *textbook of coal petrology*, Gebruder Borntraeger Verlagsbuchhandlung, Stuttgart, Germany.  
560
- 561 Tyson, R. V., 1995. Organic facies and palynofacies, In: *Sedimentary organic matter*, Springer Netherlands,  
562 pp. 81-118  
563
- 564 Teichmüller, M., 1986. Organic petrology of source rocks, history and state of the art. *Organic Geochemistry*  
565 10, 581-599.  
566
- 567 Tuinstra, F., Koenig, J. L., 1970. Raman spectrum of graphite. *The Journal of Chemical Physics* 53, 1126-  
568 1130
- 569 Vandenbroucke, M., Largeau, C., 2007. Kerogen origin, evolution and structure. *Organic Geochemistry* 38,  
570 719-833.  
571
- 572 Wilkins, R. W., Boudou, R., Sherwood, N., Xiao, X., 2014. Thermal maturity evaluation from inertinites by  
573 Raman spectroscopy: The 'RaMM' technique. *International Journal of Coal Geology* 128, 143-152.  
574
- 575 Wopenka, B., Pasteris, J. D., 1993. Structural characterization of kerogens to granulite-facies graphite:  
576 applicability of Raman microprobe spectroscopy. *The American Mineralogist* 78, 533-557.  
577
- 578 Yui, T. F., Huang, E., Xu, J., 1996. Raman spectrum of carbonaceous material: a possible metamorphic grade  
579 indicator for low-grade metamorphic rocks. *Journal of Metamorphic Geology* 14, 115-124.  
580
- 581 Zhou, Q., Xiao, X., Pan, L., Tian, H., 2014. The relationship between micro-Raman spectral parameters and  
582 reflectance of solid bitumen. *International Journal of Coal Geology* 121, 19-25.  
583

#### 584 **Figure captions**

585  
586  
587  
588 Figure 1. Examples of Raman spectra measured on organic matter extracted from cuttings at different  
589 stratigraphic depth. The stratigraphic column is redrawn after Schito et al. (2016)  
590  
591

592 Figure 2. Example of bands and bands position obtained by Raman analysis on dispersed organic matter for:  
593 low matured samples collected at the top of the well (a) and high matured samples collected at the bottom of  
594 the well (b)

595  
596 Figure 3. Trends with depth of: position of the D band (a), position of the G band (b), difference between G  
597 band and D band positions (c), width at half height of the D band (d), the width at half height of the G band  
598 (e), intensities ratios between D and G bands (f), area ratios between D and G bands(g), full width at  
599 maximum height of the D and G bands (h), RA1 parameter (i) and RA2 parameter (j).

600 Grey dots indicate terrestrial derived organic matter rich kerogen, black dots amorphous organic matter rich  
601 kerogen. Bars indicate standard deviation for each samples

602

603 Figure 4 Correlation between  $R_o\%_{eq}$ , calculated based on clay mineralogy and FT-IR analyses and distance  
604 between D and G band (a), width at half height of the G band (b), area ratio between D and G bands (c); RA2  
605 parameter (d) and width ratio between D and G ratio (e)

606

607

608 Figure 5. Schematic evolution of the GI and the G bands

609

610 Figure 6. Ratio of G intensity against: S band area (a), DI band area (b), D band area (c) and Dr band area (d)  
611 for all sample (not average per each depth) of the analysed well

612

613 Figure 7. Evolution of the Raman spectra from high metamorphic stages to the immature stage of HC  
614 generation. Raman spectra for temperatures higher than 170 °C are redrawn from Lahfid et al. (2010) and  
615 Beyssac et al. (2002). Temperature for samples from this work were carried out from thermal model by  
616 Schito et al. (2016).

617

618 Table 1. Organic matter composition and Raman parameters for each depth interval analysed. Acronyms:  
619 AOM amorphous organic matter; MPH marine phytoplankton; CHF continental herbaceous fragments; CWF  
620 continental wooden fragments; stdv: standard deviation; pD: position of the D band ( $\text{cm}^{-1}$ ); pG: position of  
621 the G band ( $\text{cm}^{-1}$ ); wD: full width at maximum height of the D band ( $\text{cm}^{-1}$ ); wG: full width at maximum  
622 height of the D band ( $\text{cm}^{-1}$ );  $\Delta$  D-G: difference between G band and D band position ( $\text{cm}^{-1}$ ); ID/IG: intensity  
623 ratio between D and G bands; aD/aG: area ratio between D and G bands; RA1: area (S+DI+D) / area  
624 (S+DI+D+Dr+GI+G); RA2: area (S+DI+D) / area (Dr+GI+G); wD/wG: ratio between full width at  
625 maximum height of D and G bands; s.d: standard deviation



# Diagenetic thermal evolution of organic matter by Raman spectroscopy

Andrea Schito <sup>a</sup>, Claudia Romano <sup>a</sup>, Sveva Corrado <sup>a</sup>, Domenico Grigo <sup>b</sup>, Brent Poe <sup>c</sup>

<sup>a</sup> Dipartimento di Scienze, Sezione di Scienze Geologiche, Università degli Studi Roma Tre, L.go S. Leonardo Murialdo 1, 00146, Roma, Italy

<sup>b</sup> Eni SpA e Exploration & Production Division, Via Emilia, San Donato Milanese, MI, 20097, Italy

<sup>c</sup> Dipartimento di Geotecnologie per l'Ambiente ed il Territorio, Università degli Studi "G. d'Annunzio" – Chieti, Via dei Vestini 30, 66013 Chieti Scalo, Italy

## Corresponding author.

E-mail address: [andrea.schito@uniroma3.it](mailto:andrea.schito@uniroma3.it)

**Keywords:** thermal maturity; dispersed organic matter; Raman spectroscopy; diagenesis

## Abstract

Vitrinite reflectance is considered one of the most reliable indicators of thermal maturity in sedimentary basins and is widely used to calibrate numerical models that assess hydrocarbon generation/expulsion from source rocks. Nevertheless, ambiguities in vitrinite reflectance can occur from variations in composition and preservation state of organic facies, temperature/ pressure conditions and the abundance of organic matter resulting in incorrect or uncertain assessments of petroleum systems.

This study presents an original application of Raman spectroscopy to assess the diagenesis - catagenesis of kerogen between the immature and mid-mature stages of hydrocarbon generation. Kerogens were isolated from 33 intervals of drill cuttings from a 5 km thick Oligocene-Miocene siliciclastic section of the Malembo Formation (Lower Congo Basin, Angola). Their Raman spectra were obtained and derived parameters were compared to depth and to previously reported equivalent vitrinite reflectance values. The best correlations between thermal maturity and Raman parameters were found for D-G band distance; FWHM of the G band; D/G area ratio; RA2 ratio (calculated as S+DI+SD/Dr+Gl+G band ratio) and the D/G width ratio. The Raman parameters were not influenced by varying kerogen composition (mixed type II/III). The technique offers the potential to reduce the risk of source rock thermal maturity assessment even when organic facies rich in amorphous organic matter are present.

## 1 Introduction

Quantitative evaluation of the thermal maturity of organic matter (OM) dispersed in sediments is a key element in assessing the processes of hydrocarbon (HC) generation/expulsion in petroleum systems. It is linked to the thermal evolution of sedimentary basins and orogenic belts (Corrado et al., 2010; Allen and Allen, 2013; Hackley and Cardott, 2016). Vitrinite reflectance analysis is considered a highly reliable and

37 reproducible measure of thermal maturity of coals. Its application to organic matter dispersed in sediments is  
38 a common practice, but there are inherent limitations that can lower the accuracy of the measurement. In  
39 many marine sediments, primary vitrinite macerals are absent or very sparse and it is often difficult to obtain  
40 good results without interference from eroded, secondary sources. Vitrinite reflectance in dispersed organic  
41 matter can also be effected by other processes such as oxidation during transport, preservation, and  
42 retardation and/or suppression. Numerical models calibrated against ambiguous vitrinite reflectance data can  
43 yield inaccurate or biased results. Alternative analytical techniques based on the analysis of both the organic  
44 and inorganic fraction of sediments can minimize these limitations (e.g., Aldega et al. 2007; Corrado et al.,  
45 2009; Federici et al., 2010; Di Paolo et al., 2012; Cantarelli et al., 2013; Andreucci et al., 2014; Schito et al.,  
46 2016).

47 Raman spectroscopy is a potential powerful non-destructive tool to quantitatively evaluate thermal maturity  
48 of organic matter (e.g., Beyssac et al., 2002; Quirico et al., 2005; Guedes et al., 2010, 2012; Lahfid et al.,  
49 2010; Liu et al., 2012, Hinrichs et al., 2014; Wilkins et al., 2014; Zhou et al., 2014; Lünsdorf, 2016; Mum  
50 and Inan, 2016; Ferralis et al., 2016). Advances in instrumentation and data processing have spurred  
51 increased applications, and the technique is now simple, fast and can be performed directly on standard  
52 petrographic thin sections or on bulk kerogen.

53 Specifically, two bands on Raman spectra, namely G (graphitic) and D (disordered), are related to the growth  
54 of the ordered domains with respect to the disordered ones in the organic matter (Tuinstra & Koenig, 1970).  
55 Parameters linked to D and G bands have been used to show reliable correlations with paleotemperatures  
56 between 200 °C and 650 °C (Wopenka and Pasteris, 1993; Beyssac et al., 2002; Aoya et al., 2010; Lahfid et  
57 al., 2010; Endo et al., 2012) and against thermal maturity between 1 and 5-6 R<sub>o</sub>% (Kelemen and Fang, 2001;  
58 Jehlička et al., 2003; Quirico et al., 2005; Guedes et al., 2010; 2012; Liu et al., 2012; Hinrichs et al., 2014;  
59 Wilkins et al., 2014; Zhou et al., 2014; Lünsdorf, 2016; Mum and Inan, 2016).

60 The range of thermal maturity spanning the diagenetic to mid-catagenetic stages (corresponding to R<sub>o</sub>% 0.4-  
61 1.2) has been explored systematically in only a few studies (Wilkins et al., 2014; Hinrichs et al., 2016;  
62 Lünsdorf, 2016). These report considerable uncertainties at the low maturity stages, which are usually the  
63 most critical in constraining basin models.

64 In this study, we examine the applicability of Raman spectroscopy as a thermal indicator in the range  
65 between the immature and middle mature stages of HC generation, when applied to type II/III kerogen  
66 composed mainly of amorphous organic matter (AOM). We present the procedures and analytical results of  
67 the first order Raman spectra performed on Cenozoic organic matter dispersed in sediments of the Malembo  
68 Formation drilled in Lower Congo Basin (Angola) that records this maturity range. We demonstrate that  
69 robust parameterization of the thermal maturity of dispersed organic matter is possible using Raman  
70 indicators.

71

72

73 **2 Methods and Materials**

74 *2.1 Kerogen and thermal maturity*

75 Kerogen is the insoluble macromolecular fraction of sedimentary organic matter (Vandenbroucke and  
76 Largeau, 2007) and is the precursor of oil and gas resources. Dispersed OM is usually highly heterogeneous  
77 and reflects differences in its origin and preservation state. Different classifications of kerogen exist, based  
78 on optical analyses performed in reflected and transmitted light or rooted on bulk parameters, such as H/C  
79 and O/C atomic ratios or Hydrogen and Oxygen indexes derived from pyrolysis yields and TOC values.

80 In this work, we mainly refer to classifications based on optical organic petrography using transmitted light  
81 microscopy (Teichmüller, 1986; Tyson, 1995). Kerogen composition is classified into four classes from  
82 which the abundance and distribution of hydrogen-rich macerals can be discerned: 1) AOM: amorphous  
83 organic matter; 2) MPH: marine phytoplankton; 3) CWF: continental woody organic matter, namely  
84 phytoclasts; and 4) CHF: continental herbaceous fragments.

85 Analyses were performed on 33 samples originating from cuttings taken from a 5000 meter thick section  
86 drilled offshore Angola (Malembó Formation - Lower Congo Basin). The succession ranges from Oligocene  
87 to Upper Miocene and is composed mainly of organic-rich shales interbedded by nearshore to deepwater  
88 sandstones (Schito et al., 2016).

89 Organic matter of different origin and preservation state, detected through transmitted light analyses, were  
90 found in the upper section of the well (depth: 1290-3360m) where woody fragments (CWF) and herbaceous  
91 fragments (CHF) of terrigenous origin coexist with amorphous organic matter (AOM) and marine  
92 phytoplankton (MPH). In contrast, the lower part of the well (depth: 3600-4950 m) is mainly composed of  
93 amorphous organic matter with traces of bitumen (Table 1, Schito et al., 2016). Reflected light analyses on  
94 kerogen indicate that organic matter of woody fragments of continental origin are represented by vitrinite  
95 group macerals, whereas inertinite group macerals are totally absent (Table 1, Schito et al., 2016).

96 The maturation pattern of the well ranges between about 0.35 and 1.5 expressed as vitrinite reflectance  
97 values ( $R_o\%$ ) as reported in Corrado et al. (2016) and Schito et al. (2016).

98

99 *2.2 Sample preparation*

100 Kerogens were extracted using a wet-chemical acid demineralization technique according to Robl and Davis  
101 (1993) and Schimmelmann et al. (1999). Samples were lightly ground in an agate mortar for about 1 minute.  
102 Carbonates were dissolved by adding HCl on the dried samples. The HCl was added in small increments to  
103 prevent excessive foaming. Digestion of remaining silicates was done by adding a mixture composed in equal  
104 parts by distilled water and HF concentrated at 40% weight percent (45 ml) to 5 g of sample and placed on a  
105 shaker table for 2 hours. Kerogen isolates plus any acid-resistant minerals were recovered and washed 5-6 times  
106 with distilled water.

107

108 *2.3 Raman Spectroscopy and curve fitting*

109 Raman spectroscopy was performed on the kerogen isolates using a Jobin Yvon micro-Raman LabRam system  
110 in a backscattering geometry. Data were collected over the range of 700-2300  $\text{cm}^{-1}$  (first order Raman

111 spectrum) using a 600 grooves/mm spectrometer gratings and CCD detector. A Neodimium-Yag laser at 532 nm  
112 (green laser) was used as the light source and optical filters adjusted the power of the laser (<0.4mW). The  
113 Raman backscattering was recorded after an integration time of 20 seconds for 6 repetitions for each  
114 measurement. This, together with the use of green laser and optical filters, allowed us to reduce the fluorescence  
115 background to minimal values. Between ten and fifteen measurements were performed for each samples to  
116 ensure reproducibility of measurements. Each organic grain was analysed with a 2  $\mu\text{m}$  diameter spot using a  
117 50 $\times$  optical power objective.

118 Raman spectra of highly disordered carbon materials, are affected by interference due to high fluorescence  
119 caused by the diffuse presence of hydrogen or residual mineral matter. The first step in the analysis of the  
120 spectra is the removal of the high fluorescence background by a baseline subtraction procedure. Once the  
121 procedure is optimized, it then must be reproduced for the entire set of samples.

122 Baseline subtraction was performed using a third order polynomial curve that best followed the real trend of the  
123 fluorescence in the most immature samples with high fluorescence background. In order to avoid errors induced  
124 by differences in the spectra range considered by the subtraction, we fixed baseline points at 1000 and 1850  $\text{cm}^{-1}$   
125 for all spectra. A polynomial curve was chosen with respect to the linear baseline because the latter tends to  
126 overestimate the D and G peaks intensities. We observed that the maximum difference resulting from baseline  
127 correction was detected for the D band intensity, whose values tend to be higher by 10-15 %.

128 After removal of the background, the spectra were deconvoluted using LabSpec 6 software by Horiba. As the  
129 Raman spectra of OM in diagenetic conditions show broad overlapping bands and multiple curve-fitting  
130 solutions exist (Lünsdorf and Lünsdorf, 2016), we found that the best solution using the minimum number of  
131 components was attained using a six band deconvolution with a mixed Gaussian-Lorentzian band profile. The  
132 goodnessof fit is defined by the minimum values of the  $\chi^2$  value (less than 3 according to Sadezky et al., 2005).  
133 Several attempts to use only five bands fitting systematically provided  $\chi^2$  values two or three times higher than  
134 those obtained with a six bands approach. All spectra were deconvoluted using the six peak deconvolution  
135 procedure.

136

#### 137 *2.4 Band assignment for Raman spectra in dispersed organic matter*

138 The Raman spectral signal of kerogen is recorded in a “first order” region between 1000 and 2000  $\text{cm}^{-1}$  and  
139 “second order” region between 2000 and 3500  $\text{cm}^{-1}$ . Bands in the second order region are generally hidden  
140 by fluorescence for low mature samples (Beyssac et al., 2002) and were not observed in this study. The first  
141 order Raman spectrafor carbonaceous materials consist of two main bands known as the D and G bands  
142 (Tuinstra and Koenig, 1970; Friedel and Carlson, 1972) and other bands that vary depending on the rank (Li,  
143 2007; Potgieter-Vermaak et al., 2011). The G band is the only Raman active vibration in crystalline graphite  
144 at 1582  $\text{cm}^{-1}$  (Tuinstra and Koenig, 1972; Reich and Thomsen, 2004; Pimenta, 2007) and is related to the in-  
145 plane vibration of the carbon atoms in the graphene sheets.

146 The D band at 1350  $\text{cm}^{-1}$  becomes active in disordered graphite and its frequency depends on the excitation  
147 laser (Pócsik et al., 1998). Its origin has been interpreted as a results of a double resonant Raman scattering

148 process (Pócsik et al., 1998; Reich and Thomsen, 2004; and Pimenta et al., 2007). Alternatively, the  
149 collective intensity of the D band has been related to the ring breathing vibration in the graphite sub-unit or  
150 polycyclic aromatic compounds (PAHs) (Negri et al., 2002;2004; Castiglioni et al., 2004; Di Donato et al.,  
151 2004; and Lünsdorf 2016) or to aromatics with 6 rings or more (Li, 2007).

152 When dealing with disordered materials, the contribution of other spectral features at 1100-1200  $\text{cm}^{-1}$  and  
153 1400-1500  $\text{cm}^{-1}$  cannot be neglected and even the assignment of the G and D bands to graphite vibrational  
154 modes is questionable. Unfortunately, there have only been a few attempt to explain the origin of these bands  
155 in disordered materials and these studies are often contradictory (Nemanich and Solin, 1979; Beny-Bassez  
156 and Rouzaud, 1985; Ferrari and Robertson, 2000; Castiglioni et al. 2004; Negri et al., 2004; Li et al., 2007;  
157 Rebelo et al. 2016). For this reason the assignment of Raman bands for disordered material is still a matter of  
158 debate.

159 In high-rank coals, Beyssac et al. (2002) observed the presence of two additional bands in the Raman  
160 spectrum: the D2 band, appearing as a right end shoulder of the G band at approximately 1620  $\text{cm}^{-1}$  and the  
161 D3 band, a wide band residing at approximately 1500  $\text{cm}^{-1}$ . These bands have been attributed to out-of-plane  
162 defects from tetrahedral carbons (Bèny-Bassez and Rouzaud, 1985), or to small crystallite size (Nemanich  
163 and Solin, 1979). Working on carbon material matured at lower temperatures (about 200-320°C), Lahfid et  
164 al. (2010) and Sadezky et al. (2005) proposed the presence of an additional band called D4 at about 1200  $\text{cm}^{-1}$ ,  
165 attributed to  $\text{sp}^3\text{-sp}^2$  bonds or C–C and C=C stretching vibrations of polyene-like structures.

166 In a recent study, Ferralis et al. (2016) found the presence of two bands as a broad shoulder of the D bands,  
167 called D4 at 1150  $\text{cm}^{-1}$  and D5 at 1250  $\text{cm}^{-1}$ . In Ferralis et al.'s (2016) work, the two bands have been related  
168 to CH species in aliphatic hydrocarbon chains. The authors confirm this hypothesis by showing a strong  
169 correlation between the intensity of D5 or D5+D4 band with the increase of the atomic ratio H:C in the range  
170 between almost pure graphite (H:C = 0.01) and weak metamorphosed kerogen (H:C = 0.65).

171 In low maturity coals, the Raman spectra of highly disordered carbonaceous matter are more complex.

172 In Li et al. (2006) and Li (2007), Raman spectra were deconvoluted into 10 bands. The authors attributed a  
173 band at about 1700  $\text{cm}^{-1}$  (G1 band) to a carbonyl group C=O, while the Gr (1540  $\text{cm}^{-1}$ ), V1 (1465  $\text{cm}^{-1}$ ) and  
174 Vr band (1380  $\text{cm}^{-1}$ ) which represent the “overlap” between D and G were assigned to mainly amorphous  
175 carbon structures in char, especially smaller ring systems (e.g., with 3-5 fused benzene rings). At lower  
176 wavenumbers, they found that the S band (1185  $\text{cm}^{-1}$ ), together with Sl band (~1220  $\text{cm}^{-1}$ ), acts as the  
177 shoulder of the D band (1230  $\text{cm}^{-1}$ ) and mainly represents  $\text{C}_{\text{aromatic}}\text{-C}_{\text{alkyl}}$ , aromatic (aliphatic) ethers, C–C on  
178 hydroaromatic rings, hexagonal diamond carbon  $\text{sp}^3$  and C–H on aromatic rings. Finally, the Sr band (1060  
179  $\text{cm}^{-1}$ ) is assigned to C-H on aromatic rings and the R band (960-800  $\text{cm}^{-1}$ ) to C-C on alkanes and cyclic  
180 alkanes and/or C-H on aromatic rings.

181 Similarly, based on analyses of carbon nanotubes, Rebelo et al. (2016) proposed new assignments for the first  
182 order Raman spectra. In their work the G band is fitted with a Lorentzian shape at ~1580  $\text{cm}^{-1}$  surrounded by a  
183 Lorentzian Gr peak at ~1610  $\text{cm}^{-1}$  and a Gaussian G1 peak near 1500  $\text{cm}^{-1}$ . G1 band correspond to the same  
184 vibration of the G band in low size aromatic (Heise et al., 2009). The “D region” is deconvoluted to a central

185 Lorentzian D band at 1350 cm<sup>-1</sup> and two satellites Gaussian band called D<sub>l</sub> and D<sub>r</sub> (left and right) respectively at  
186 ~1250 and ~1400 cm<sup>-1</sup> that were assigned to identical vibrations of the D band, but in low size aromatic  
187 domains. Finally, a further band, the S band, was used to fit a relatively small feature on the left side of the  
188 spectra at around 1120cm<sup>-1</sup>.

189 Bands S and G<sub>1</sub> were assigned to a fingerprint of polyacetylene-like structures or areas of conjugated double  
190 bonds mainly present along the borders of structures where aromaticity has been broken upon functionalization  
191 (Shirakawa et al., 1973).

192

### 193 *2.5 Raman thermal maturity parameters*

194 Debate still exists on how to relate Raman spectral features to carbonization ranks at low thermal maturity levels  
195 (Rantish et al., 2016). Tuinstra and Koenig (1970) proposed the relation  $ID/IG = C(vL)/La$  (TK relation), to  
196 study the thermal evolution of carbonaceous materials. ID/IG is the ratio between the intensities of the D and G  
197 peaks,  $La$  is the lateral dimension (parallel to the graphene planes) of the nanocrystal and  $C(vL)$  is a constant  
198 which depends on the laser frequency. Taking IG as a reference value, which is independent of the size of the  
199 crystal (Cançado et al., 2008), Tuinstra and Koenig (1970) found an inverse relation between the intensities of  
200 the D band and the crystal dimensions. Following the TK correlation, Wopenka & Pasteris (1993) correlated  
201 certain Raman parameters with metamorphic zonation as determined by mineral assemblages.

202 Subsequently, Yui et al. (1996) demonstrated the high sensitivity of some Raman parameters to metamorphic  
203 grade from low-grade to greenschist facies, while Beyssac et al. (2002) developed the so called RSCM  
204 geothermometer (Raman Spectroscopy of Carbonaceous Material). RSCM, which expresses a relationship  
205 between the Raman parameter R<sub>2</sub> ( $R_2 = D/([G + D + D_2]$  area ratio) and metamorphic temperature, was  
206 initially calibrated in a range between 330-640°C, and later extended to contact- metamorphic rocks (Aoya et  
207 al., 2010) and low-grade metamorphism (Lahfid et al., 2010, RA1 and RA2 parameters; Lünsdorf, 2016).

208 Given the low temperature interval covering the sub-bituminous coal to the anthracite ranks, spectral features  
209 and carbonization are not so clearly correlated. In general, FWHM, positions of the G and D bands and D/G area  
210 ratio are the most sensitive parameters to maturation (Sadezky et al., 2005; Jehlicka et al., 2009; Marques et al.,  
211 2009; Guedes et al., 2010; Zhou et al., 2014; Hinrichs et al., 2016; Lünsdorf, 2016). Romero-Sarmiento et al.  
212 (2014) suggested that the FWHM of the G band shows the best correlation against Rock-Eval T<sub>max</sub> values in a  
213 set of samples from the Barnett shales (US), and Liu et al. (2012) determined thermal maturity by using the D-G  
214 distance in mature to highly mature carbonized samples of solid organic matter.

215

216

## 217 **3 Results**

### 218 *3.1 Raman spectra*

219 From a first qualitative assessment of spectral features, we observed a regular decrease of the fluorescence  
220 signal, resulting in the reduction of the slope of the spectra (Fig. 1), and a corresponding narrowing of the G  
221 bands along the same trend. We refer to Rebelo et al. (2016) for band nomenclature. Position and bands names

222 are shown in Figure 2a for low maturity OM and in Figure 2b for high maturity OM. Best fit results were  
223 achieved by considering S, DI and Dr as purely Gaussian, and D, G and GI as more mixed Gaussian-Lorentzian  
224 functions. Generally, in response to increasing thermal maturity, the width of the G band decreases, the D-G  
225 peak position difference increases and the GI area decreases.

226

### 227 3.2 Correlation of Raman parameters against thermal maturity - Malembo Formation

228 To correlate spectral features with thermal maturity, the following parameters were calculated: D and G  
229 position, D-G distance, full width at half maximum of the D and G bands (FWHM) and D/G intensity, area and  
230 full width at maximum height ratio. Moreover, we redefined the parameters RA1 and RA2 following the work  
231 of Lahfid et al. (2010), calculated as follows:

232 1)  $RA1 = \text{area}(S+DI+D) / \text{area}(S+DI+D+Dr+GI+G)$ ;

233 2)  $RA2 = \text{area}(S+DI+D) / \text{area}(Dr+GI+G)$ .

234 The D band position decreases slightly with depth from about 1380  $\text{cm}^{-1}$  to 1360  $\text{cm}^{-1}$ , while the G band position  
235 (Fig. 3a) shows no trends with depth, ranging between 1590  $\text{cm}^{-1}$  and 1600  $\text{cm}^{-1}$  (Fig. 3b). As a consequence, the  
236 D-G difference increases slightly with depth from about 220  $\text{cm}^{-1}$  to 240  $\text{cm}^{-1}$  (Fig 3c).

237 The full width at half maximum (FWHM) of the D band ranges between 90  $\text{cm}^{-1}$  and 110  $\text{cm}^{-1}$  with no defined  
238 trend, while the full width at half maximum (FWHM) of the G band decreases from about 90  $\text{cm}^{-1}$  to 55  $\text{cm}^{-1}$   
239 (Fig.3d-e). The intensity ratio between the D and G bands does not show any correlation with depth (Fig. 3f),  
240 while the D/G area ratio and full width at maximum height ratio shows a trend of increasing values with depth,  
241 ranging from about 0.5 to 1.0 and 1.0 and 1.8, respectively (Fig. 3g-h). Both RA1 and RA2 show values ranging  
242 from 0.35 to 0.50 for RA1 and from about 0.55 to 1.10 for RA2 (Fig. 3i-j). The best correlations with depth are  
243 provided by the D-G difference (Fig. 3c), the FWHM of peak G (Fig. 3e), the D/G area ratio (Fig. 3g), D/G  
244 width ratio (Fig. 3h) and the RA2 parameter (Fig. 3j).

245 We plotted these parameters against the maturity profile of the well expressed in  $R_o\%$  (for details see Schito  
246 et al., 2016) in Fig. 4. A power equation was used to fit the D/G area ( $R^2 = 0.93$ ), RA2 ( $R^2 = 0.95$ ) and D/G  
247 width ( $R^2 = 0.96$ ) parameters (Fig.4c-d-e), FWHM-G parameter ( $R^2 = 0.91$ ) and the D-G distance ( $R^2 = 0.94$ )  
248 were fitted according to a second order polynomial equation (Fig. a-b).

249

250

## 251 4 Discussions

252 We observed good correlations between Raman parameters and well depth for kerogens from the Cenozoic  
253 Malembo Formation (Lower Congo Basin, Angola) in our study. The Raman parameters also correlate very  
254 well with vitrinite reflectance values reported by Schito et al. (2016), which range from about 0.3% to about  
255 1.5%  $R_o$ . In the investigated well, Raman spectral features vary continuously with depth independent of  
256 kerogen composition. This is in general agreement with Chen et al. (2012) who showed that differences in  
257 parameters derived from micro-FT-IR analyses on vitrinite and liptinite macerals (e.g., AOM) were

258 negligible. Raman spectra parameters that best correlate against thermal maturity are: 1) D and G band  
259 position difference; 2) G band FWHM and 3) D and G bands area/width ratio (including the RA2 parameter).

260

#### 261 *4.1 Distance between D and G bands*

262 The shift in position of the D and G bands is related to processes that occur at different carbonization ranks.  
263 According to Ferrari and Robertson (2000), the D band shift toward lower wavenumbers is attributable to the  
264 increase of larger aromatic clusters passing from disordered to more ordered materials.

265 The increase of the D-G distance with thermal maturity is mainly driven by the shift of the D position toward  
266 lower wavenumbers (Fig. 3a), while no apparent trend is visible for the G position (Figure 3b). This  
267 observations are in agreement with those made others (Ferrari and Robertson, 2000; Kelemen and Fang,  
268 2001; Nestler et al., 2003; Quirico et al., 2005; Guedes et al., 2010; and Liu et al, 2012). The D-G distance is  
269 one of the best parameters to correlate against vitrinite reflectance (Fig. 4a). Our results are in agreement  
270 with Kelemen and Fang (2001) and Liu et al. (2012) (for samples with R<sub>o</sub>% varying between 0.5% and 4%).

271

#### 272 *4.2 Full Width at Half Maximum of the G band*

273 According to Ferrari and Robertson (2000), the width of the G peak increases as a function of the bond-angle disorder at  
274 sp<sup>2</sup> sites (in aromatic rings and olefinic) and its values are the greatest for high sp<sup>3</sup> sites content (aliphatic chains) in  
275 highly disordered materials. This parameter increases as a function of decreasing temperature or thermal maturity in  
276 regional metamorphism (Beyssac et al., 2002; Lahfid et al., 2010) and progressive coalification (Ferrari and Robertson,  
277 2000; Kelemen and Fang, 2001; Jehlička et al., 2003; Quirico et al., 2005; Marques et al., 2009; Guedes et al., 2010a ;  
278 Wilkins et al., 2014, Hinrichs et al., 2016). In agreement with existing studies, we observed a decrease of FWHM-G as  
279 a function of increasing R<sub>o</sub>% (Figs. 4b). According to spectra deconvolution, the overall decrease in the  
280 integrated intensity of the G region is attributable to both a decrease in the FWHM of the G band and to a  
281 decrease in area of the GI band (Fig. 5). This is in good agreement with the assignment of the GI band to  
282 polyacetylene-like structures (e.g., polyene chains) which are expected to decrease as thermal maturity  
283 increases (Castiglioni et al., 2004; Rebelo et al., 2016). Similar behaviour is seen in the Gr (1540 cm<sup>-1</sup>) and  
284 VI (1465 cm<sup>-1</sup>) of Li et al. (2007), assigned to mainly amorphous carbon structures in char, especially smaller  
285 ring systems (e.g., with 3-5 fused benzene rings) which also are expected to decrease as thermal maturity  
286 increases.

287

#### 288 *4.3 Area and width ratio parameters (D/G area, RA2, D/G width)*

289 The intensity ratio between D and G bands, is related to the in-plane crystallite size (Tuinstra and Koenig,  
290 1976) in disordered graphite and shows an inverse correlation against paleotemperatures between 330-650  
291 °C (Beyssac et al., 2002). The same relationship is not seen at low temperatures (Ferrari and Robertson,  
292 2000) and the area ratio of D and G bands and parameters related to this ratio (RA1 and RA2, Lahfid et al.,  
293 2010) correlate better against temperature and thermal maturity (Kelemen and Fang, 2001; Jehlička et al.,  
294 2003; Quirico et al., 2005; Sadezky et al., 2005; Marques et al., 2009; Guedes et al., 2010; Liu et al., 2012).



295 This is probably due to the fact that while the intensity ratio behaves similarly to the D/G area ratio for  
296 disordered graphite, this correlation is no longer valid for amorphous carbon where the width of both bands  
297 are related to the disorder in the structure (Ferrari and Robertson, 2000).

298 We observe that the ID/IG ratio does not correlate with depth (Fig. 3f) or  $R_o\%$  while D/G area and width  
299 ratio (Figs. 3g) and RA1 and RA2 parameters (Figs. 3i - j) increase linearly with thermal maturity. The  
300 increase in D/G area and width ratio and in RA1 and RA2 parameters are partially attributable to the thinning  
301 of the G band due to the clustering of the aromatic rings (Ferrari and Robertson, 2000; Li et al., 2007) and  
302 also to the decrease in intensity of peak G1 (Fig. 5). However, other contributions may also be important to  
303 consider. For this reason, in order to understand and isolate the contribution of each single band to the  
304 RA1 and RA2 variation in our set of samples, we normalized each band to the G band intensity in Figure 6,  
305 where the ratio between the G band intensity and the area of the D, S, D1 and Dr bands against an increasing  
306 maturation pattern on the x axes is presented. No significant variations are observed in the IG/S area or in the  
307 IG/D1 area ratio, while a decrease in the IG/D area (e.g., D area band increase) and an increase of the IG/Dr  
308 area ratio (e.g., Dr band area decrease) are clearly visible.

309 We conclude that the increase in RA2 ratio is attributed to the decrease in width and intensity of G and G1  
310 bands and to the decrease of the satellite band Dr. This is accompanied by a corresponding increase in D  
311 band area (IG/D area decrease) which is mostly due to an increase in FWHM of the D band (Fig 3d).

312 While the D band increases, the G, G1 and Dr decrease with increasing structural ordering, in agreement with  
313 the interpretations already proposed by Ferrari and Robertson (2000), Li et al., (2007) and Rebelo et al.  
314 (2015). The interpretation of the Dr and S bands is not straightforward. Rebelo et al. (2015) assign these  
315 bands (S and D1) to the same vibrational modes and to the same structural units of G1 and Dr bands,  
316 respectively; thus, we would expect similar coupled behaviour for these bands at increasing temperature.

317 However, we observe a decoupling between S and G1 and D1 and Dr bands with temperature.

318 A similar decoupling was observed by Ferralis et al. (2016) who suggested a different origin for the S and D1  
319 bands (called the D4 and D5 bands in Ferralis et al., 2016). The authors observed that in the  $1200\text{ cm}^{-1}$  -  $1300$   
320  $\text{cm}^{-1}$  region the D4 and D5 bands are related to deformation modes of C-C (D4) and CH (D5) species  
321 associated with long saturated and unsaturated alkane chains. These bands show an intensity increase with  
322 the increase of H:C ratio from weakly metamorphosed kerogen to graphite.

323 On the other hand, no trend is observed for the S and D1 bands in Figure 6. This could be due to the different  
324 composition of the OM in the upper part of the well (varying terrigenous OM and AOM enrichment)  
325 generating different responses of the excitation bands with increasing thermal maturity. The variation of C-C  
326 and C-H associated with aliphatic at low maturity stages ( $R_o\% < 1.5$ ) is not straightforward and depends on  
327 complex chemical changes that occur simultaneously, such as shortening of aliphatic chains, decreased  
328 branching of aliphatic chains and formation of cyclic compounds (Lis et al., 2005). Therefore, we infer that  
329 the assignment of the S and D1 bands is still unclear and further investigations are strongly needed to fully  
330 address this issue.

331

### 332 4.3 Raman spectra evolution in Organic matter

333 Comparing our results with those obtained at higher degrees of maturation (Beyssac et al., 2002; Lahfid et  
334 al., 2010 and Rantish et al., 2016), we can trace the evolution of Raman spectra of the OM over a wide range  
335 of paleotemperatures. Using data from previous studies, we observed the following changes going from  
336 anthracite to graphite ranks (i.e. typically greenschist facies and above, see Wopenka and Pasteris, 1993;  
337 Beyssac et al., 2002): a decrease in the D band area, a shrinking of the G band and a shift of the G band  
338 toward the triperiodic graphite position (Fig. 7). Conversely, going from low volatile bituminous coal to  
339 anthracite ranks, we observed from the works of Lahfid et al., (2010), Hinrichs et al., (2016) and Lünsdorf,  
340 (2016) an increase of the D band and a progressive disappearance of the minor bands. From results from this  
341 work, we found that changes in Raman spectra in diagenesis consist mainly in a narrowing of the G band  
342 region and a small increase of the D band area. The decrease of the G band area is due to a progressive  
343 shrinking of the G band and to the decrease in the area of the G1 and Dr bands assigned to small aromatic  
344 rings and small polyene domains present only in kerogen at low thermal maturity levels (Castiglioni et al.,  
345 2004; Li et al., 2007; Rebelo et al., 2016).

346

347

### 348 5 Conclusions

349 Raman spectroscopic measurements were performed on shales collected from a 5 km deep well drilled across  
350 the Miocene-Oligocene Malembo Formation in the Lower Congo Basin (offshore of Angola). Bulk kerogens,  
351 with a thermal maturity range increasing from about 0.3 R<sub>o</sub>% at the top of the well to about 1.5 R<sub>o</sub>% at the  
352 bottom were analysed.

353 The best correlations of Raman spectral parameters against the increase of thermal maturity are: D-G band  
354 distance; FWHM of the G band; D/G area ratio; RA2 ratio (calculated as S+D1+SD/Dr+G1+G band ratio) and  
355 the D/G width ratio.

356 These results demonstrate that, at low diagenetic stages (between the immature and mid-mature stages of  
357 hydrocarbon generation) changes in Raman spectra of undifferentiated dispersed organic matter show  
358 quantifiable changes in response to thermal maturation and can be used to successfully parameterize the  
359 thermal evolution of a sedimentary succession.

360

### 361 Acknowledgments

362 We are greatly indebted to ENI for providing cuttings analysed in this work and permission to publish  
363 transmitted light analysis data on kerogen. Organic matter analyses were performed at the EVPL and ALBA  
364 (Roma Tre University) and at the ENI laboratories of Bolgiano (S. Donato Milanese). Donato Barbieri, Lea  
365 di Paolo and Roberto Galimberti (ENI) are kindly acknowledged for stimulating discussions on organic  
366 matter thermal evolution. This research was funded by: MIUR grants to Roma Tre PhD School in Earth  
367 Sciences (XXVIII doctoral cycle, 2013-2015).

368

369

### 370 References

371

372 Aldega, L., Corrado, S., Grasso, M., Maniscalco, R., 2007. Correlation of diagenetic data from organic and  
373 inorganic studies in the Apenninic-Maghrebian fold-and-thrust belt: a case study from eastern Sicily. *The*  
374 *Journal of Geology* 115, 335-353.  
375

376 Allen, P. A., Allen, J. R., 2013. *Basin Analysis: Principles and Application to Petroleum Play Assessment*,  
377 third ed. John Wiley & Sons, Hoboken, NJ, USA.  
378

379 Andreucci, B., Castelluccio, A., Corrado, S., Jankowski, L., Mazzoli, S., Szaniawski, R., Zattin, M., 2015.  
380 Interplay between the thermal evolution of an orogenic wedge and its retro-wedge basin: An example from  
381 the Ukrainian Carpathians. *Geological Society of America Bulletin* 127, 410-427.  
382

383 Aoya, M., Kouketsu, Y., Endo, S., Shimizu H., Mizukami, T., Nakamura, D., Wallis, S., 2010. Extending the  
384 applicability of the Raman carbonaceous-material geothermometer using data from contact metamorphic  
385 rocks. *Journal of Metamorphic Geology* 28, 895-914.  
386

387 Beny-Bassez, C., Rouzaud, J., 1985. Characterization of carbonaceous materials by correlated electron and  
388 optical microscopy and Raman microspectroscopy. *Scanning Electron Microscopy* 1, 119-132.  
389

390 Beyssac, O., Goffé, B., Chopin, C., Rouzaud, J., 2002. Raman spectra of carbonaceous material in  
391 metasediments: a new geothermometer. *Journal of metamorphic Geology* 20, 859-871.  
392

393 Beyssac, O., Goffé, B., Petitet, J.-P., Froigneux, E., Moreau, M., Rouzaud, J.-N., 2003. On the  
394 characterization of disordered and heterogeneous carbonaceous materials by Raman spectroscopy.  
395 *Spectrochimica Acta Part A: Molecular and Biomolecular Spectroscopy* 59, 2267-2276.  
396

397 Cançado, L., Takai, K., Enoki, T., Endo, M., Kim, Y., Mizusaki, H., Speziali, N., Jorio, A., Pimenta, M.,  
398 2008. Measuring the degree of stacking order in graphite by Raman spectroscopy. *Carbon* 46, 272-275.  
399

400 Cantarelli, V., Aldega, L., Corrado, S., Invernizzi, C., Casas-Sainz, A., 2013. Thermal history of the Aragón-  
401 Béarn Basin (Late Paleozoic, western Pyrenees, Spain); insights into basin tectonic evolution. *Italian Journal*  
402 *of Geosciences* 132, 443-462.  
403

404 Caricchi, C., Corrado, S., Di Paolo, L., Aldega, L., Grigo, D., 2016. Thermal maturity of Silurian deposits in  
405 the Baltic Syneclise (on-shore Polish Baltic Basin): contribution to unconventional resources assessment.  
406 *Italian Journal of Geosciences* 135, 383-393.  
407

408 Carr, A.D., 2000. Suppression and retardation of vitrinite reflectance, Part 1. Formation and significance for  
409 hydrocarbon generation. *Journal of Petroleum Geology* 23, 313-343.  
410

411 Castiglioni, C., Tommasini, M., Zerbi, G., 2004. Raman spectroscopy of polyconjugated molecules and  
412 materials: confinement effect in one and two dimensions: *Philosophical Transactions of the Royal Society of*  
413 *London. Series A. Mathematical, Physical and Engineering Sciences* 362, 2425-2459.  
414

415 Corrado, S., Aldega, L., Balestrieri, M.L., Maniscalco, R., Grasso, M., 2009. Structural evolution of the  
416 sedimentary accretionary wedge of the Alpine system in eastern Sicily: thermal and thermochronological  
417 constraints. *Geological Society of America Bulletin* 121, 1475-1490.  
418

419 Corrado, S., Aldega, L., Zattin, M., 2010. Sedimentary vs. tectonic burial and exhumation along the  
420 Apennines (Italy). *Journal of the Virtual Explorer* 36,1-37.  
421

422 Corrado, S., Schito, A., Aldega, L., Grigo, D., 2016. A quantitative multi-method approach to assess thermal  
423 evolution of the Lower Congo Basin (Angola). *Rendiconti Online della Società Geologica Italiana* 40,  
424 pp.525.  
425

426 Di Paolo, L., Aldega, L., Corrado, S., Mastalerz, M., 2012. Maximum burial and unroofing of Mt. Judica  
427 recess area in Sicily: implication for the Apenninic–Maghrebian wedge dynamics. *Tectonophysics* 530, 193-  
428 207.

429

430 Di Donato, E., Tommasini, M., Fustella, G., Brambilla, L., Castiglioni, C., Zerbi, G., Simpson, C.D., Müllen,  
431 K., Negri, F., 2004. Wavelength-dependent Raman activity of D<sub>2h</sub> symmetry polycyclic aromatic  
432 hydrocarbons in the D-band and acoustic phonon regions. *Chemical Physics* 301, 81–93.

433

434 Endo, S., Wallis, S. R., Tsuboi, M., Torres De Leòn, R., Solari, L. A., 2012. Metamorphic evolution of  
435 lawsonite eclogites from the southern Motagua fault zone, Guatemala: insights from phase equilibria and  
436 Raman spectroscopy. *Journal of Metamorphic Geology* 30, 143-164.

437

438 Federici, I., Cavazza, W., Okay, A. I., Beyssac, O., Zattin, M., Corrado, S. Dellisanti, F., 2010.  
439 Thermal Evolution of the Permo-Triassic Karakaya Subduction-accretion Complex between the Biga  
440 Peninsula and the Tokat Massif (Anatolia). *Turkish Journal of Earth Sciences* 19, 409-429.

441

442 Ferrari, A.C., Robertson, J., 2000. Interpretation of Raman spectra of disordered and amorphous carbon:  
443 *Physical Review B* 61, 14095-14107.

444

445 Ferrari, A. C., Robertson, J., 2004. Raman spectroscopy of amorphous, nanostructured, diamond-like  
446 carbon, and nanodiamond. *Philosophical Transactions of the Royal Society of London A: Mathematical,*  
447 *Physical and Engineering Sciences* 362, 2477-2512.

448

449 Friedel, R., Carlson, G., 1972. Difficult carbonaceous materials and their infra-red and Raman spectra.  
450 Reassignments for coal spectra. *Fuel* 51, 194-198.

451

452 Guedes, A., Valentim, B., Prieto, A. C., Rodrigues, S., Noronha, F., 2010. Micro-Raman spectroscopy of  
453 collotelinite, fusinite and macrinite. *International Journal of Coal Geology* 83, 415-422.

454

455 Guedes, A., Valentim, B., Prieto, A., Noronha F., 2012. Raman spectroscopy of coal macerals and fluidized  
456 bed char morphotypes. *Fuel* 97, 443-449.

457

458 Hackley, P. C., Cardott, B. J., 2016. Application of organic petrography in North American shale petroleum  
459 systems: A review. *International Journal of Coal Geology* 163, 8-51.

460

461 Heise, H., Kuckuk, R., Ojha, A., Srivastava, A., Srivastava, V., Asthana, B., 2009. Characterisation of  
462 carbonaceous materials using Raman spectroscopy: a comparison of carbon nanotube filters, single-and  
463 multi-walled nanotubes, graphitised porous carbon and graphite. *Journal of Raman Spectroscopy* 40, 344-  
464 353.

465

466 Jehlička, J., Urban, O., Pokorný, J., 2003. Raman spectroscopy of carbon and solid bitumens in sedimentary  
467 and metamorphic rocks. *Spectrochimica Acta Part A: Molecular and Biomolecular Spectroscopy* 59, 2341-  
468 2352.

469

470 Jehlička, J., Šťastná, A., Přikryl, R., 2009. Raman spectral characterization of dispersed carbonaceous matter  
471 in decorative crystalline limestones. *Spectrochimica Acta Part A: Molecular and Biomolecular Spectroscopy*  
472 73, 404-409.

473

474 Kelemen, S., Fang, H., 2001, Maturity trends in Raman spectra from kerogen and coal. *Energy & Fuels* 15,  
475 653-658.

476

477 Lahfid, A., Beyssac, O., Deville, E., Negro, F., Chopin, C., Goffé, B., 2010. Evolution of the Raman  
478 spectrum of carbonaceous material in low-grade metasediments of the Glarus Alps (Switzerland). *Terra*  
479 *Nova* 22, 354-360.

480

481 Li, C.-Z., 2007. Some recent advances in the understanding of the pyrolysis and gasification behaviour of  
482 Victorian brown coal. *Fuel* 86, 1664-1683.  
483

484 Lis, G. P., Mastalerz, M., and Schimmelmann, A., 2008, Increasing maturity of kerogen type II reflected by  
485 alkylbenzene distribution from pyrolysis-gas chromatography–mass spectrometry: *Organic Geochemistry* 39,  
486 440-449.  
487

488 Liu, D., Xiao, X., Tian, H., Min, Y., Zhou, Q., Cheng, P., Shen, J., 2012. Sample maturation calculated using  
489 Raman spectroscopic parameters for solid organics: Methodology and geological applications. *Chinese*  
490 *Science Bulletin* 58, 1285-1298.  
491

492 Lünsdorf, N. K., 2016. Raman spectroscopy of dispersed vitrinite - Methodical aspects and correlation with  
493 reflectance. *International Journal of Coal Geology* 153, 75-86.  
494

495 Marques, M., Suárez-Ruiz, I., Flores, D., Guedes, A., Rodrigues, S., 2009. Correlation between optical,  
496 chemical and micro-structural parameters of high-rank coals and graphite. *International Journal of Coal*  
497 *Geology* 77, 377-382.  
498

499 Mumm, A. S., İnan, S., 2016. Microscale Organic Maturity determination of Graptolites using  
500 Raman Spectroscopy. *International Journal of Coal Geology* 162, 96-107.  
501

502 Negri, F., di Donato, E., Tommasini, M., Castiglioni, C., Zerbi, G., Müllen, K., 2004. Resonance Raman  
503 contribution to the D band of carbon materials: modeling defects with quantum chemistry. *Journal of*  
504 *Chemical Physics* 120, 11889–11900.  
505

506 Nemanich, R., Solin, S., 1979. First-and second-order Raman scattering from finite-size crystals of graphite.  
507 *Physical Review B* 20, 392.  
508

509 Nestler, K., Dietrich, D., Witke, K., Rößler, R., Marx, G., 2003. Thermogravimetric and Raman  
510 spectroscopic investigations on different coals in comparison to dispersed anthracite found in permineralized  
511 tree fern *Psaronius* sp. *Journal of Molecular Structure* 661, 357-362.  
512

513 Petersen, H., Rosenberg, P., 1998. Reflectance retardation (suppression) and source rock properties related to  
514 hydrogen enriched vitrinite in middle Jurassic coals, Danish North Sea. *Journal of Petroleum Geology* 21,  
515 247-263.  
516

517 Potgieter-Vermaak, S., Maledi, N., Wagner, N., Van Heerden, J., Van Grieken, R., Potgieter, J., 2011.  
518 Raman spectroscopy for the analysis of coal: a review. *Journal of Raman Spectroscopy* 42, 123-129.  
519

520 Pócsik, I., Hundhausen, M., Koós, M., Ley, L., 1998. Origin of the D peak in the Raman spectrum of  
521 microcrystalline graphite. *Journal of Non-Crystalline Solids* 227, 1083-1086.  
522

523 Price, L. C., Barker, C. E., 1985. Suppression of vitrinite reflectance in amorphous rich kerogen--a major  
524 unrecognized problem. *Journal of Petroleum Geology* 8, p. 59-84.  
525

526 Quirico, E., Rouzaud, J. N., Bonal, L., Montagnac, G., 2005. Maturation grade of coals as revealed by  
527 Raman spectroscopy: progress and problems. *Spectrochimica Acta Part A: Molecular and Biomolecular*  
528 *Spectroscopy* 61, 2368-2377.  
529

530 Rantitsch, G., Lämmerer, W., Fisslthaler, E., Mitsche, S., Kaltenböck, H., 2016. On the discrimination of  
531 semi-graphite and graphite by Raman spectroscopy. *International Journal of Coal Geology* 159, 48–56.  
532

533 Rebelo, S. L., Guedes, A., Szcfczyk, M. E., Pereira, A. M., Araújo, J. P., Freire, C., 2016. Progress in the  
534 Raman spectra analysis of covalently functionalized multiwalled carbon nanotubes: unraveling disorder in  
535 graphitic materials. *Physical Chemistry Chemical Physics* 18, 12784-12796.  
536

- 537 Robl, T. L., Davis, B. H., 1993. Comparison of the HF-HCl and HF-BF<sub>3</sub> maceration techniques and the  
538 chemistry of resultant organic concentrates. *Organic Geochemistry* 20, 249-255.  
539
- 540 Romero-Sarmiento, M.-F., Rouzaud, J.-N., Bernard, S., Deldicque, D., Thomas, M., Littke, R., 2014.  
541 Evolution of Barnett Shale organic carbon structure and nanostructure with increasing maturation. *Organic*  
542 *Geochemistry* 71, 7-16.  
543
- 544 Sadezky, A., Muckenhuber, H., Grothe, H., Niessner, R., Pöschl, U., 2005. Raman microspectroscopy of  
545 soot and related carbonaceous materials: Spectral analysis and structural information. *Carbon* 43, 1731-1742.  
546
- 547 Schito, A., Corrado, S., Aldega, L., Grigo, D., 2016. Overcoming pitfalls of vitrinite reflectance  
548 measurements in the assessment of thermal maturity: the case history of the lower Congo basin. *Marine and*  
549 *Petroleum Geology* 74, 59-70.  
550
- 551 Scott, A. C., Glasspool, I. J., 2007. Observations and experiments on the origin and formation of inertinite  
552 group macerals. *International Journal of Coal Geology* 70, 53-66.  
553
- 554 Shirakawa, H., Ito, T., Ikeda, S., 1973. Raman scattering and electronic spectra of poly (acetylene). *Polymer*  
555 *Journal* 4, 460-462.  
556
- 557 Taylor, G. H., 1998. *Organic petrology: A new handbook incorporating some revised parts of Stach's*  
558 *textbook of coal petrology*, Gebruder Borntraeger Verlagsbuchhandlung, Stuttgart, Germany.  
559
- 560 Tyson, R. V., 1995. Organic facies and palynofacies, In: *Sedimentary organic matter*, Springer Netherlands,  
561 pp. 81-118  
562
- 563 Teichmüller, M., 1986. Organic petrology of source rocks, history and state of the art. *Organic Geochemistry*  
564 10, 581-599.  
565
- 566 Tuinstra, F., Koenig, J. L., 1970. Raman spectrum of graphite. *The Journal of Chemical Physics* 53, 1126-  
567 1130
- 568 Vandenbroucke, M., Largeau, C., 2007. Kerogen origin, evolution and structure. *Organic Geochemistry* 38,  
569 719-833.  
570
- 571 Wilkins, R. W., Boudou, R., Sherwood, N., Xiao, X., 2014. Thermal maturity evaluation from inertinites by  
572 Raman spectroscopy: The 'RaMM' technique. *International Journal of Coal Geology* 128, 143-152.  
573
- 574 Wopenka, B., Pasteris, J. D., 1993. Structural characterization of kerogens to granulite-facies graphite:  
575 applicability of Raman microprobe spectroscopy. *The American Mineralogist* 78, 533-557.  
576
- 577 Yui, T. F., Huang, E., Xu, J., 1996. Raman spectrum of carbonaceous material: a possible metamorphic grade  
578 indicator for low-grade metamorphic rocks. *Journal of Metamorphic Geology* 14, 115-124.  
579
- 580 Zhou, Q., Xiao, X., Pan, L., Tian, H., 2014. The relationship between micro-Raman spectral parameters and  
581 reflectance of solid bitumen. *International Journal of Coal Geology* 121, 19-25.  
582

#### 583 **Figure captions**

584 **Figure 1.** Examples of Raman spectra measured on organic matter extracted from cuttings at different  
585 stratigraphic depth. The stratigraphic column is redrawn after Schito et al. (2016)  
586

587

588

589

590

591 Figure 2. Example of bands and bands position obtained by Raman analysis on dispersed organic matter for:  
592 low matured samples collected at the top of the well (a) and high matured samples collected at the bottom of  
593 the well (b)

594  
595 Figure 3. Trends with depth of: position of the D band (a), position of the G band (b), difference between G  
596 band and D band positions (c), width at half height of the D band (d), the width at half height of the G band  
597 (e), intensities ratios between D and G bands (f), area ratios between D and G bands(g), full width at  
598 maximum height of the D and G bands (h), RA1 parameter (i) and RA2 parameter (j).

599 Grey dots indicate terrestrial derived organic matter rich kerogen, black dots amorphous organic matter rich  
600 kerogen. Bars indicate standard deviation for each samples

601

602 Figure 4 Correlation between  $R_o\%_{eq}$ , calculated based on clay mineralogy and FT-IR analyses and distance  
603 between D and G band (a), width at half height of the G band (b), area ratio between D and G bands (c); RA2  
604 parameter (d) and width ratio between D and G ratio (e)

605

606

607 Figure 5. Schematic evolution of the GI and the G bands

608

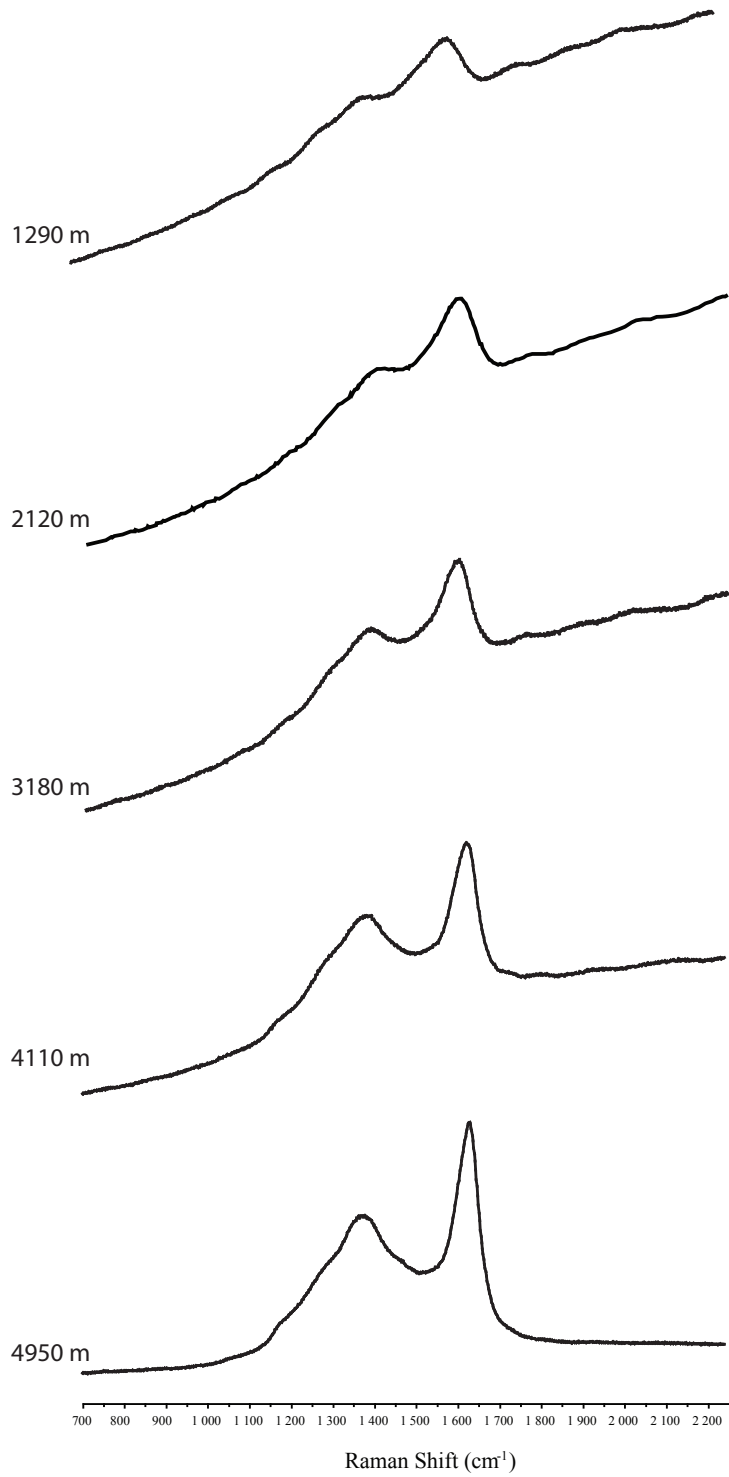
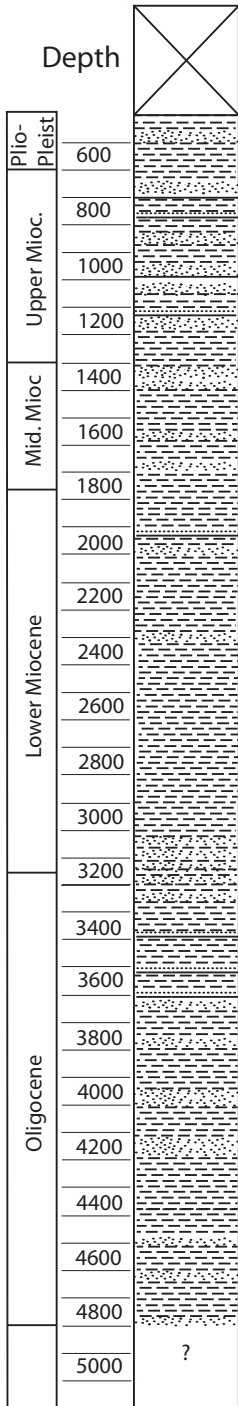
609 Figure 6. Ratio of G intensity against: S band area (a), DI band area (b), D band area (c) and Dr band area (d)  
610 for all sample (not average per each depth) of the analysed well

611

612 Figure 7. Evolution of the Raman spectra from high metamorphic stages to the immature stage of HC  
613 generation. Raman spectra for temperatures higher than 170 °C are redrawn from Lahfid et al. (2010) and  
614 Beyssac et al. (2002). Temperature for samples from this work were carried out from thermal model by  
615 Schito et al. (2016).

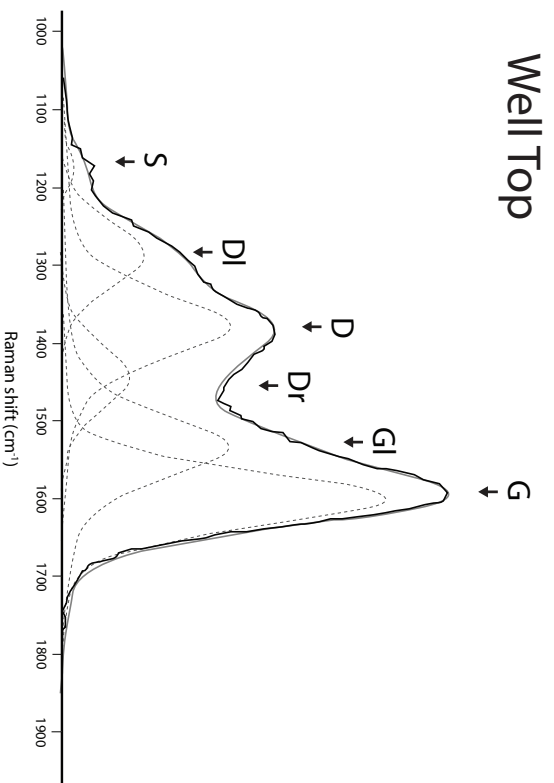
616

617 Table 1. Organic matter composition and Raman parameters for each depth interval analysed. Acronyms:  
618 AOM amorphous organic matter; MPH marine phytoplankton; CHF continental herbaceous fragments; CWF  
619 continental wooden fragments; stdv: standard deviation; pD: position of the D band ( $\text{cm}^{-1}$ ); pG: position of  
620 the G band ( $\text{cm}^{-1}$ ); wD: full width at maximum height of the D band ( $\text{cm}^{-1}$ ); wG: full width at maximum  
621 height of the D band ( $\text{cm}^{-1}$ );  $\Delta$  D-G: difference between G band and D band position ( $\text{cm}^{-1}$ ); ID/IG: intensity  
622 ratio between D and G bands; aD/aG: area ratio between D and G bands; RA1: area (S+DI+D) / area  
623 (S+DI+D+Dr+GI+G); RA2: area (S+DI+D) / area (Dr+GI+G); wD/wG: ratio between full width at  
624 maximum height of D and G bands; s.d: standard deviation

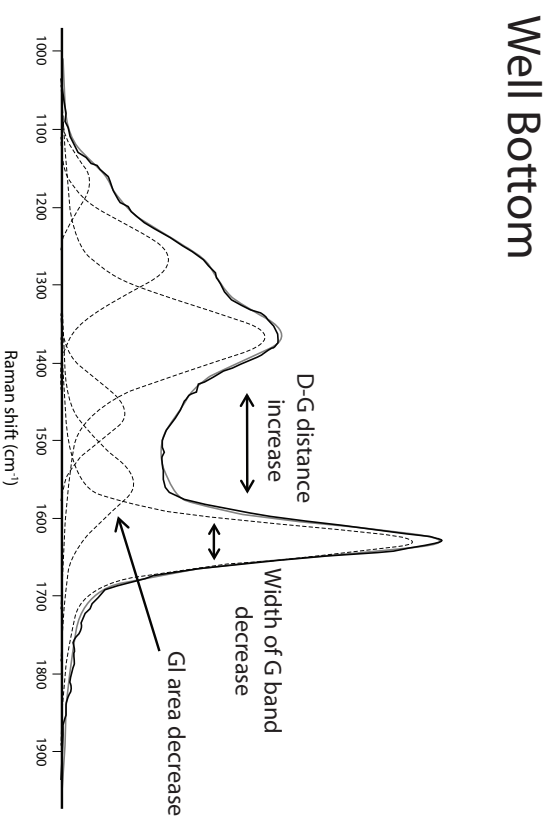


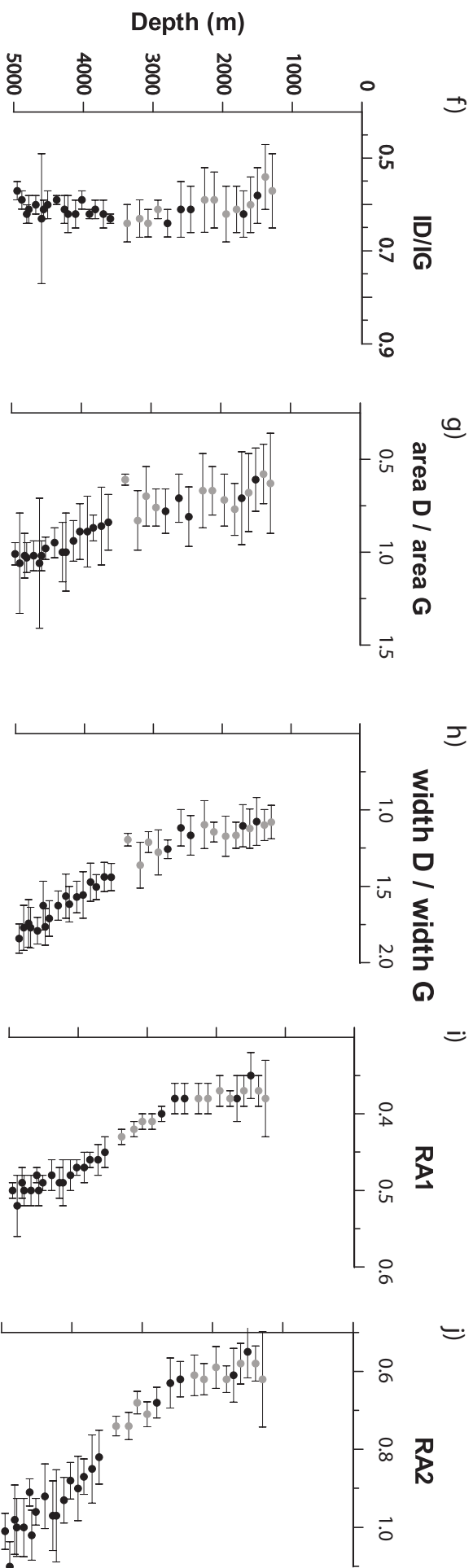
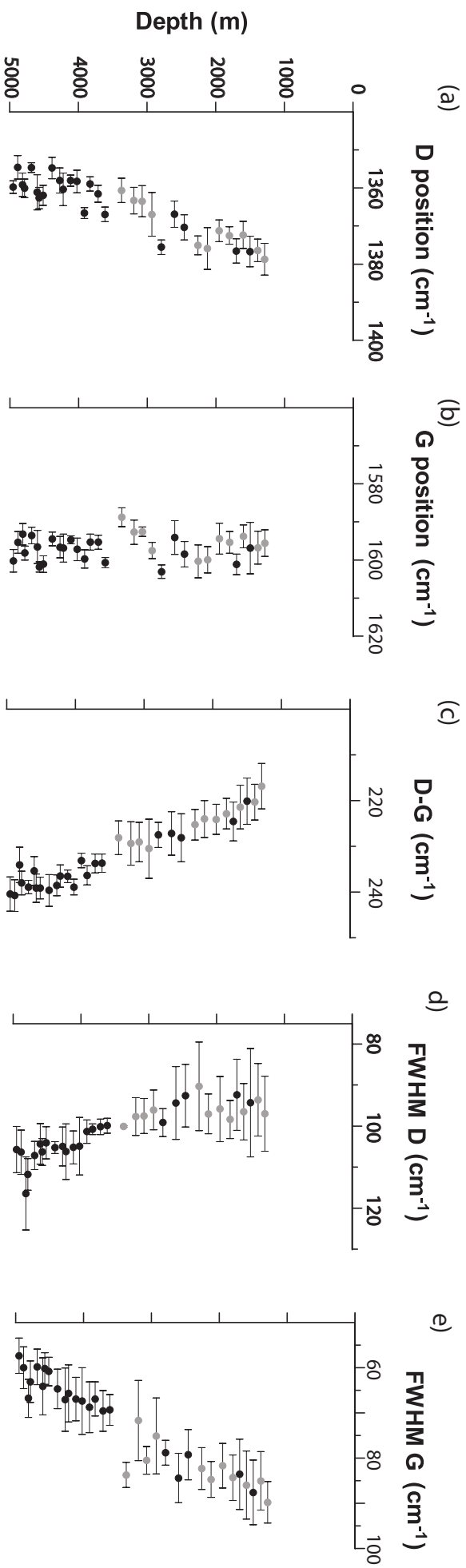


a)

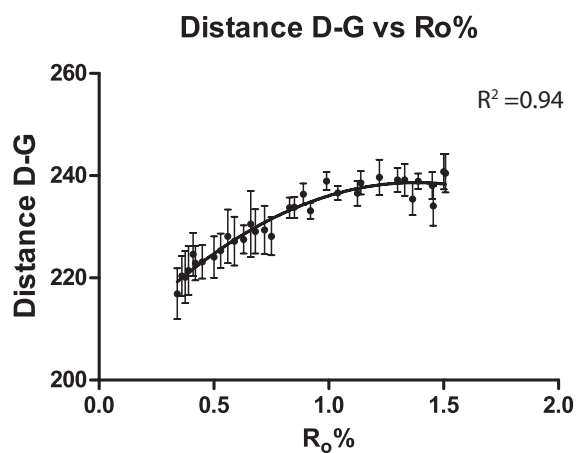


b)

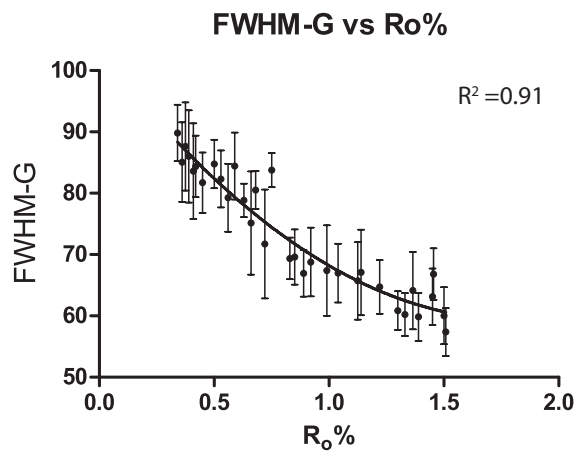




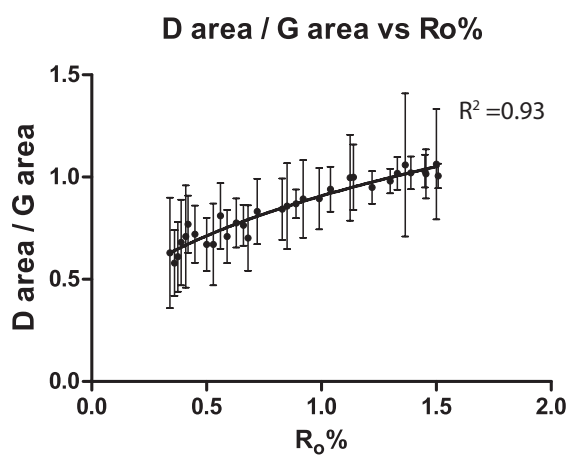
a)



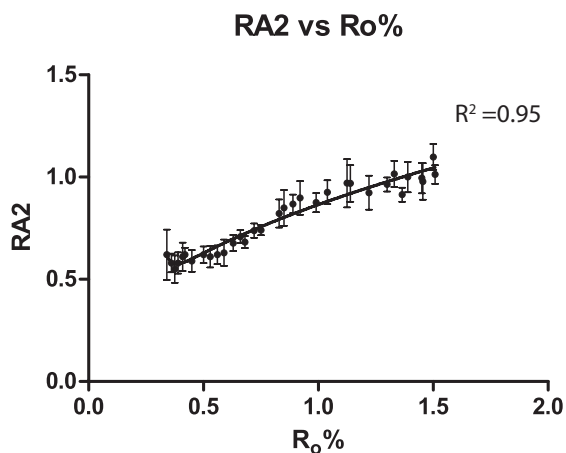
b)



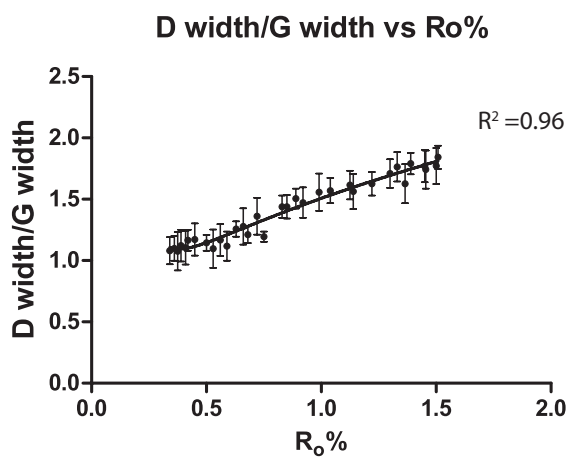
c)



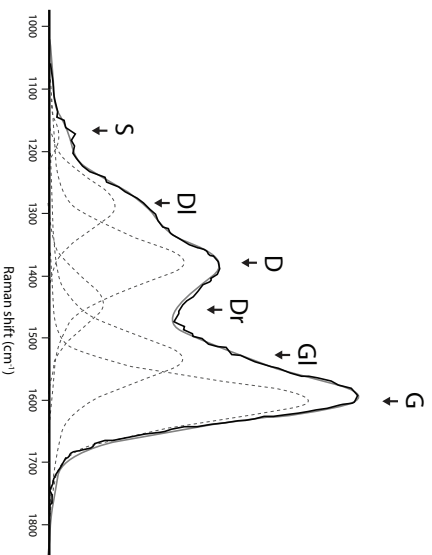
d)



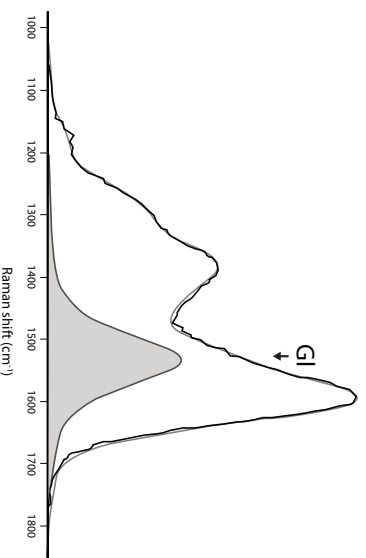
e)



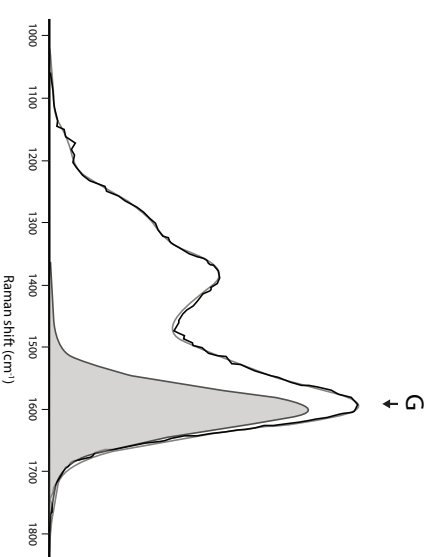
Low thermal maturity signal



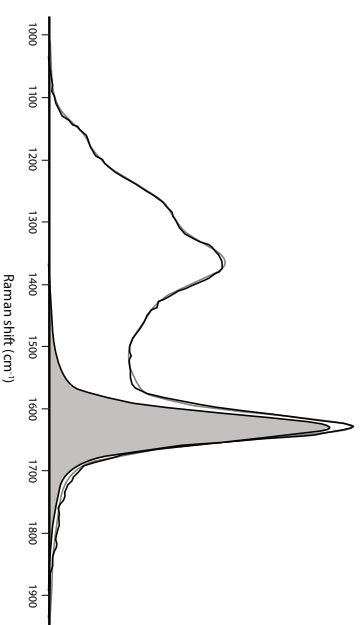
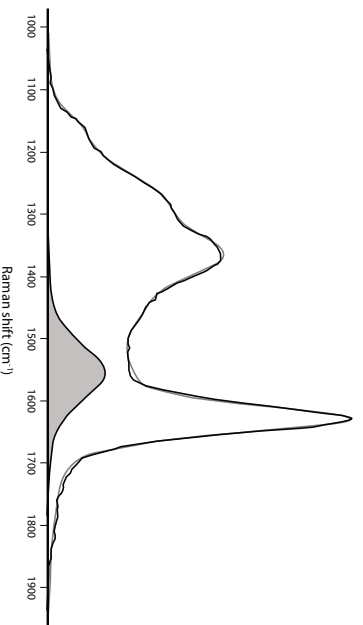
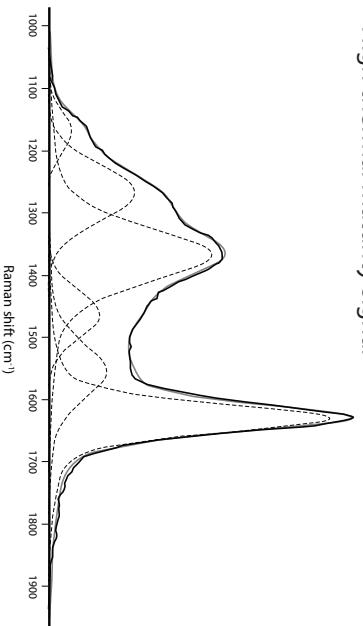
G1 band area

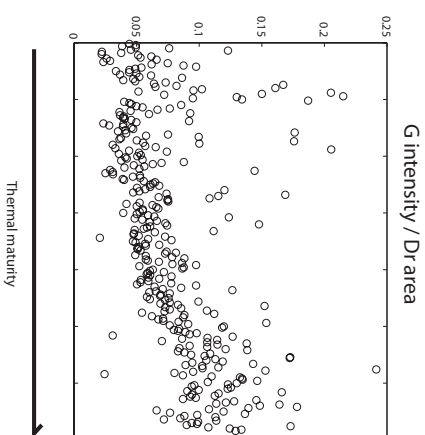
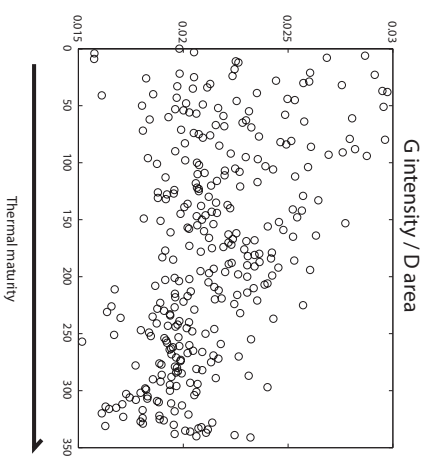
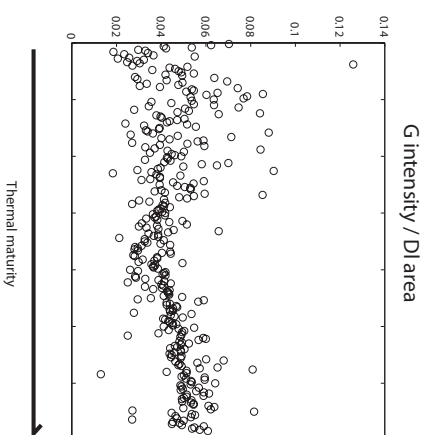
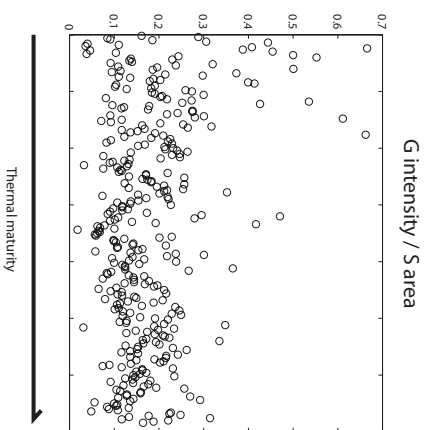


Width at half height of G band

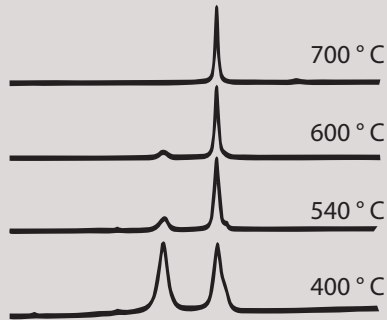


High thermal maturity signal





*Epizone*  
Beyssac et al., 2002



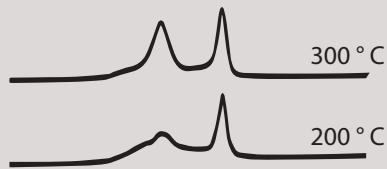
### Coal ranks

Antracite to Graphite

### Driven mechanism with Temperature increase

Decrease of the D band area and decrease of the full width at maximum height of the G band

*Anchizone*  
Lahfid et al., 2010



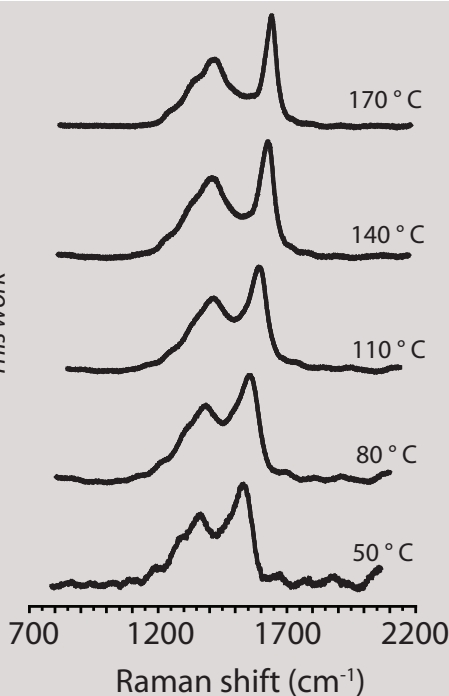
### Coal ranks

Low volatile bituminous coal to antracite

### Driven mechanism with Temperature increase

Increase of the D band area and progressive disappearance of the minor bands

*Diagenesis*  
This work



### Coal ranks

Subbituminous coals to medium volatile bituminous coal

### Driven mechanism with Temperature increase

Decrease of the G band area due to a progressive shirking of the G band and to the decreases in the area of the DI band assigned by recent work (Rebelo et al., 2016) to small aromatic rings and small polyene domains present only in kerogene at lo thermal maturity

Depth (m)	Kerogen composition	pD	s. d. pD	pG	s. d. pG	wD	s. d. wD	wG	s. d. wG	Δ D -G	s. d. Δ D-G
1290	AOM <sub>10</sub> CHP <sub>25</sub> CWF <sub>65</sub>	1378.71	4.14	1595.58	3.48	96.96	9.15	89.82	4.60	1378.33	4.97
1390	AOM <sub>5</sub> MPH <sub>15</sub> CHP <sub>30</sub> CWF <sub>60</sub>	1376.38	2.98	1596.75	4.34	93.57	8.84	85.07	6.48	1376.02	3.91
1500	AOM <sub>80</sub> CHP <sub>15</sub> CWF <sub>5</sub>	1376.70	4.01	1596.85	6.73	94.29	13.22	87.63	7.18	1376.35	5.08
1600	AOM <sub>70</sub> CHP <sub>20</sub> CWF <sub>10</sub>	1372.34	3.54	1593.79	3.02	96.48	6.85	86.00	7.53	1371.98	4.79
1700	AOM <sub>70</sub> CHP <sub>25</sub> CWF <sub>5</sub>	1376.55	3.18	1601.14	2.69	92.35	8.66	83.61	7.78	1376.17	4.23
1800	AOM <sub>10</sub> MPH <sub>5</sub> CHP <sub>25</sub> CWF <sub>60</sub>	1372.48	2.30	1595.36	2.84	98.37	4.65	84.37	5.02	1372.09	3.34
1950	AOM <sub>20</sub> MPH <sub>10</sub> CHP <sub>25</sub> CWF <sub>45</sub>	1371.25	2.86	1594.40	4.04	95.80	7.94	81.72	4.94	1370.87	3.28
2120	AOM <sub>60</sub> CHP <sub>15</sub> CWF <sub>25</sub>	1375.91	5.47	1599.96	3.45	97.02	4.85	84.76	3.96	1375.53	4.05
2260	AOM <sub>10</sub> MPH <sub>10</sub> CHP <sub>15</sub> CWF <sub>65</sub>	1375.04	2.46	1600.35	4.29	90.29	10.81	82.33	4.64	1374.66	3.36
2460	AOM <sub>80</sub> MPH <sub>5</sub> CHP <sub>10</sub> CWF <sub>5</sub>	1370.33	3.32	1598.46	3.35	92.54	7.64	79.28	5.55	1369.95	5.25
2600	AOM <sub>90</sub> CHP <sub>5</sub> CWF <sub>5</sub>	1366.90	3.43	1594.10	4.40	94.35	8.88	84.44	5.47	1366.51	4.76
2790	AOM <sub>80</sub> MPH <sub>5</sub> CHP <sub>10</sub> CWF <sub>5</sub>	1375.53	1.91	1603.05	1.77	99.12	3.40	78.84	2.74	1375.13	2.75
2930	AOM <sub>40</sub> CHP <sub>20</sub> CWF <sub>40</sub>	1366.95	5.75	1597.50	2.11	96.04	4.82	75.14	8.42	1366.54	6.47
3070	AOM <sub>90</sub> CHP <sub>5</sub> CWF <sub>5</sub>	1363.48	4.10	1592.56	1.22	97.53	4.27	80.53	3.08	1363.08	4.33
3190	AOM <sub>25</sub> CHP <sub>35</sub> CWF <sub>40</sub>	1363.32	3.49	1592.70	3.16	97.67	4.59	71.74	8.87	1362.90	4.75
3370	AOM <sub>35</sub> CHP <sub>15</sub> CWF <sub>50</sub>	1360.63	3.21	1588.77	2.49	100.04	0.22	83.77	2.79	1360.20	3.71
3610	AOM <sub>60</sub> CHP <sub>25</sub> CWF <sub>15</sub>	1366.95	1.90	1600.68	1.36	99.86	1.82	69.37	3.38	1366.50	1.99
3710	AOM <sub>80</sub> MPH <sub>10</sub> CHP <sub>5</sub> CWF <sub>5</sub>	1361.53	2.21	1595.32	1.81	100.16	1.92	69.61	4.50	1361.07	2.06
3830	AOM <sub>90</sub> CHP <sub>5</sub> CWF <sub>5</sub>	1358.91	1.88	1595.29	2.12	100.73	1.30	66.94	3.78	1358.45	2.07
3910	AOM <sub>10</sub> CHP <sub>20</sub> BIT <sub>70</sub>	1366.58	1.40	1599.71	2.42	101.30	2.85	68.79	5.61	1366.11	1.57
4020	AOM <sub>85</sub> CHP <sub>15</sub>	1358.27	2.97	1597.20	2.98	104.89	7.01	67.39	7.39	1357.80	1.73
4110	AOM <sub>100</sub>	1358.07	1.45	1594.67	1.03	105.18	4.00	66.98	4.80	1357.59	1.39
4220	-	1360.34	4.27	1596.89	3.67	106.20	6.79	65.71	6.30	1359.85	2.43
4270	AOM <sub>100</sub>	1358.01	3.29	1596.61	2.79	104.93	4.76	67.08	6.99	1357.52	2.28
4380	AOM <sub>100</sub>	1354.77	2.79	1594.43	1.80	105.20	1.46	64.73	4.39	1354.29	3.47
4510	-	1361.91	2.62	1601.08	2.19	104.07	3.91	60.87	3.16	1361.42	2.37
4570	AOM <sub>100</sub>	1362.64	2.82	1601.82	1.34	106.27	3.26	60.23	3.49	1362.14	3.10
4600	AOM <sub>100</sub>	1361.13	4.60	1596.56	4.35	104.32	4.98	64.14	6.32	1360.66	3.18
4680	AOM <sub>100</sub>	1354.64	1.28	1593.58	2.16	107.15	3.44	59.84	3.93	1354.14	1.49
4780	-	1360.10	2.41	1598.16	1.82	111.75	3.88	63.13	4.61	1359.60	2.61
4810	AOM <sub>100</sub>	1359.13	3.08	1593.21	2.84	116.39	8.92	66.81	4.19	1358.63	3.87
4880	AOM <sub>100</sub>	1354.58	3.09	1595.37	2.83	106.33	5.39	60.04	4.63	1354.06	3.46
4950	-	1359.74	1.64	1600.22	2.97	105.69	5.64	57.38	3.90	1359.24	3.75

Depth (m)	Kerogen composition	ID/IG	s. d.	ID/IG	ad/ag	s. d.	ad/ag	RA1	s. d.	RA1	RA2	s. d.	RA2	WD/wG	s. d.	WD/wG
1290	AOM <sub>1.0</sub> CH <sub>2.5</sub> CF <sub>6.5</sub>	0.57	0.08	0.63	0.27	0.38	0.38	0.05	0.62	0.12	1.08	0.11				
1390	AOM <sub>5</sub> MPH <sub>5</sub> CH <sub>30</sub> CF <sub>60</sub>	0.54	0.07	0.58	0.16	0.37	0.37	0.02	0.58	0.05	1.10	0.10				
1500	AOM <sub>80</sub> CH <sub>1.5</sub> CF <sub>5</sub>	0.58	0.06	0.61	0.17	0.35	0.35	0.03	0.55	0.07	1.08	0.16				
1600	AOM <sub>70</sub> CH <sub>20</sub> CF <sub>10</sub>	0.60	0.06	0.68	0.21	0.37	0.37	0.02	0.58	0.05	1.12	0.13				
1700	AOM <sub>70</sub> CH <sub>25</sub> CF <sub>5</sub>	0.62	0.05	0.71	0.25	0.38	0.38	0.03	0.61	0.07	1.10	0.14				
1800	AOM <sub>1.0</sub> MPH <sub>5</sub> CH <sub>25</sub> CF <sub>60</sub>	0.61	0.05	0.77	0.14	0.38	0.38	0.01	0.62	0.03	1.17	0.09				
1950	AOM <sub>20</sub> MPH <sub>10</sub> CH <sub>25</sub> CF <sub>45</sub>	0.62	0.06	0.72	0.14	0.37	0.37	0.02	0.59	0.05	1.17	0.13				
2120	AOM <sub>60</sub> CH <sub>1.5</sub> CF <sub>2.5</sub>	0.59	0.06	0.67	0.13	0.38	0.38	0.02	0.62	0.04	1.14	0.06				
2260	AOM <sub>1.0</sub> MPH <sub>10</sub> CH <sub>1.5</sub> CF <sub>6.5</sub>	0.59	0.07	0.67	0.20	0.38	0.38	0.02	0.61	0.05	1.10	0.16				
2460	AOM <sub>80</sub> MPH <sub>5</sub> CH <sub>10</sub> CF <sub>5</sub>	0.61	0.05	0.81	0.16	0.38	0.38	0.02	0.62	0.05	1.17	0.13				
2600	AOM <sub>60</sub> CH <sub>5</sub> CF <sub>5</sub>	0.61	0.06	0.71	0.13	0.38	0.38	0.02	0.63	0.06	1.12	0.12				
2790	AOM <sub>80</sub> MPH <sub>5</sub> CH <sub>10</sub> CF <sub>5</sub>	0.64	0.03	0.78	0.12	0.40	0.40	0.01	0.68	0.04	1.26	0.06				
2930	AOM <sub>40</sub> CH <sub>20</sub> CF <sub>40</sub>	0.61	0.02	0.76	0.10	0.41	0.41	0.01	0.71	0.03	1.28	0.15				
3070	AOM <sub>90</sub> CH <sub>5</sub> CF <sub>5</sub>	0.64	0.03	0.70	0.16	0.41	0.41	0.01	0.68	0.03	1.21	0.07				
3190	AOM <sub>25</sub> CH <sub>35</sub> CF <sub>40</sub>	0.63	0.04	0.83	0.16	0.42	0.42	0.01	0.74	0.04	1.36	0.15				
3370	AOM <sub>35</sub> CH <sub>15</sub> CF <sub>50</sub>	0.64	0.04	0.61	0.03	0.43	0.43	0.01	0.74	0.02	1.19	0.04				
3610	AOM <sub>60</sub> CH <sub>25</sub> CF <sub>1.5</sub>	0.63	0.01	0.84	0.15	0.45	0.45	0.02	0.82	0.07	1.44	0.09				
3710	AOM <sub>80</sub> MPH <sub>10</sub> CH <sub>5</sub> CF <sub>5</sub>	0.62	0.03	0.86	0.21	0.46	0.46	0.02	0.85	0.09	1.44	0.10				
3830	AOM <sub>60</sub> CH <sub>5</sub> CF <sub>5</sub>	0.61	0.02	0.87	0.07	0.46	0.46	0.01	0.87	0.05	1.50	0.08				
3910	AOM <sub>10</sub> CH <sub>20</sub> BIT <sub>70</sub>	0.62	0.01	0.89	0.19	0.47	0.47	0.02	0.90	0.08	1.47	0.12				
4020	AOM <sub>85</sub> CH <sub>1.5</sub>	0.59	0.02	0.89	0.15	0.47	0.47	0.01	0.88	0.05	1.56	0.15				
4110	AOM <sub>100</sub>	0.62	0.03	0.94	0.11	0.48	0.48	0.02	0.93	0.06	1.57	0.10				
4220	-	0.62	0.04	1.00	0.21	0.49	0.49	0.03	0.97	0.12	1.62	0.12				
4270	AOM <sub>100</sub>	0.61	0.03	1.00	0.16	0.49	0.49	0.02	0.97	0.09	1.56	0.14				
4380	AOM <sub>100</sub>	0.59	0.01	0.95	0.08	0.48	0.48	0.02	0.92	0.08	1.63	0.10				
4510	-	0.60	0.03	0.98	0.06	0.49	0.49	0.01	0.96	0.03	1.71	0.12				
4570	AOM <sub>100</sub>	0.61	0.02	1.02	0.08	0.50	0.50	0.02	1.02	0.06	1.76	0.12				
4600	AOM <sub>100</sub>	0.63	0.14	1.06	0.35	0.48	0.48	0.01	0.91	0.03	1.63	0.16				
4680	AOM <sub>100</sub>	0.60	0.02	1.02	0.08	0.50	0.50	0.02	1.00	0.07	1.79	0.09				
4780	-	0.61	0.03	1.03	0.08	0.50	0.50	0.02	1.00	0.07	1.77	0.13				
4810	AOM <sub>100</sub>	0.62	0.02	1.02	0.12	0.49	0.49	0.02	0.98	0.09	1.74	0.16				
4880	AOM <sub>100</sub>	0.59	0.02	1.06	0.27	0.52	0.52	0.04	1.10	0.06	1.77	0.15				
4950		0.57	0.02	1.01	0.06	0.50	0.50	0.01	1.01	0.05	1.84	0.10				



## **Highlights**

- We analysed kerogen from a well from the offshore Angola with Raman spectroscopy
- Thermal maturity ranges between immature and mature stages of HC generation
- Raman parameters show good trends with depth in the well
- We found a good correlation between thermal maturity trend and Raman parameters
- We discuss the physical-chemical meaning of Raman spectra variations in diagenesis